



Published in final edited form as:

Cell Rep. 2022 March 22; 38(12): 110539. doi:10.1016/j.celrep.2022.110539.

Coupling between DNA replication, segregation, and the onset of constriction in *Escherichia coli*

Sriram Tiruvadi-Krishnan¹, Jaana Männik¹, Prathitha Kar^{2,3}, Jie Lin^{2,4}, Ariel Amir^{2,*}, Jaan Männik^{1,*}

¹Department of Physics and Astronomy, University of Tennessee, Knoxville, TN 37996, USA

²John A. Paulson School of Engineering and Applied Sciences, Harvard University, Cambridge, MA 02134, USA

³Department of Chemistry and Chemical Biology, Harvard University, Cambridge, MA 02134, USA

⁴Center for Quantitative Biology and Peking-Tsinghua Joint Center for Life Sciences, Academy for Advanced Interdisciplinary Studies, Peking University, Beijing, China

SUMMARY

Escherichia coli cell cycle features two critical cell-cycle checkpoints: initiation of replication and the onset of constriction. While the initiation of DNA replication has been extensively studied, it is less clear what triggers the onset of constriction and when exactly it occurs during the cell cycle. Here, using high-throughput fluorescence microscopy in microfluidic devices, we determine the timing for the onset of constriction relative to the replication cycle in different growth rates. Our single-cell data and modeling indicate that the initiation of constriction is coupled to replication-related processes in slow growth conditions. Furthermore, our data suggest that this coupling involves the mid-cell chromosome blocking the onset of constriction via some form of nucleoid occlusion occurring independently of SImA and the Ter linkage proteins. This work highlights the coupling between replication and division cycles and brings up a new nucleoid mediated control mechanism in *E. coli*.

Graphical abstract

This is an open access article under the CC BY-NC-ND license (<http://creativecommons.org/licenses/by-nc-nd/4.0/>).

*Correspondence: jmannik@utk.edu (J.M.), arielamir@seas.harvard.edu (A.A.).

AUTHOR CONTRIBUTIONS

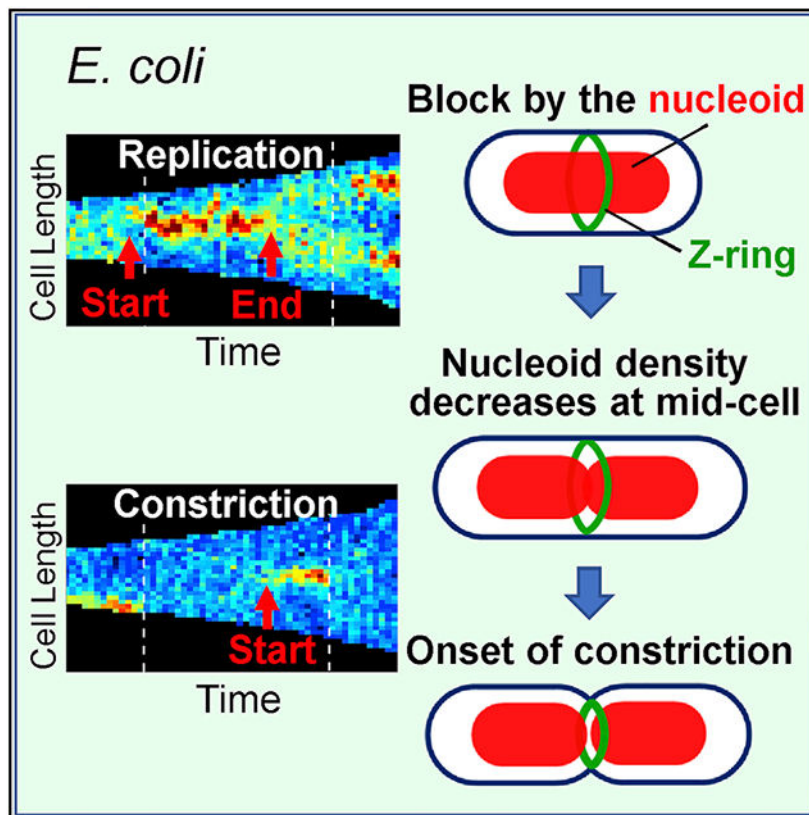
Jaana Männik, Jaan Männik, and S.T.-K. designed the experiments. Jaana Männik and S.T.-K. performed the experiments and contributed the reagents. A.A., P.K., and J.L. designed and performed the modeling. All of the authors analyzed the data and were involved in writing the manuscript.

SUPPLEMENTAL INFORMATION

Supplemental information can be found online at <https://doi.org/10.1016/j.celrep.2022.110539>.

DECLARATION OF INTERESTS

The authors declare that they have no competing interests.



In brief

Using high-throughput microscopy, Tiruvadi-Krishnan et al. determine timings for critical cell-cycle checkpoints related to division and replication in *Escherichia coli*. The data, combined with cell-cycle modeling, show that the onset of constriction is blocked by the mid-cell nucleoid. In slow-growth conditions, the blockage is limiting for cell division.

INTRODUCTION

The bacterial cell cycle involves DNA replication and division cycles (Ho et al., 2018; Willis and Huang, 2017). There is a consensus that the replication cycle in *Escherichia coli* is initiated by the binding of DnaA in its active ATP-bound form to the origin of replication (Katayama et al., 2017; Reyes-Lamothe and Sherratt, 2019). However, it is less clear what triggers the division cycle and how the division cycle is coupled to the replication cycle. It is commonly thought that cell division starts with the formation of the Z ring (Haeusser and Margolin, 2016). The latter refers to a collection of FtsZ protofilaments at the mid-cell attached to the plasma membrane via the linker proteins FtsA and ZipA (Du and Lutkenhaus, 2019). After forming the Z ring, but after considerable delay (20%–40% of the cell cycle; Aarsman et al., 2005), several additional essential proteins involved in septal cell wall synthesis and partitioning DNA between daughter compartments are recruited (de Boer, 2010; Egan et al., 2020). The recruitment of these additional proteins proceeds in an interdependent manner and culminates with the arrival of FtsN (Weiss, 2015; Liu et al.,

2015; Haeusser and Margolin, 2016; Daley et al., 2016; Du and Lutkenhaus, 2019; Boes et al., 2019). Once FtsN is recruited, a mature divisome has formed, and the cell starts to constrict at its center by synthesizing septal peptidoglycan (Weiss, 2015; Liu et al., 2015; Daley et al., 2016; Du and Lutkenhaus, 2019).

The above description may suggest that control over cell division is exerted when the Z ring forms because the signal cascade starts from this event. However, while the formation of the Z ring is a prerequisite for cell division and is known to be controlled by different cellular processes (Willis and Huang, 2017), there is evidence that a checkpoint downstream of the Z ring formation triggers the onset of the constriction. In fast growth conditions, the formation of the Z ring in daughter cells is typically coincident with the dissociation of the old Z ring in the mother cell, and as such, is not controlled by other cell-cycle processes, including replication (Männik et al., 2018). In slow growth conditions, the Z ring forms later in the cell cycle, but it initially appears only transiently (Walker et al., 2020). The transient nature of the Z ring is also inconsistent with the idea that the formation of the Z ring is a cell-cycle checkpoint with a well-defined point of no return. In contrast to the Z ring formation, once the constriction starts to form at the mid-cell, it is usually not aborted. A critical checkpoint that is rate limiting for cell division thus occurs at the initiation of constriction (Harris and Theriot, 2016).

It has been unclear whether this checkpoint is coupled to the replication cycle of the chromosome, which is the main focus of this article. As mentioned above, the onset of constriction is the effective trigger for cell division. How division is coupled to the replication cycle has been extensively studied over many decades. The prevailing view from the early studies of the cell cycle in *E. coli*, formalized in the Cooper-Helmstetter model, is that cell division follows replication termination after a fixed time (Cooper and Helmstetter, 1968). This viewpoint postulates that replication and division cycles are tightly coupled. Some recent single-cell measurements (Wallden et al., 2016) and cell-cycle modeling studies have supported this conclusion (Ho and Amir, 2015; Amir, 2014; Witz et al., 2019). However, several other works have concluded that the replication and division cycles in *E. coli* are independent of each other (Bernander and Nordstrom, 1990; Campos et al., 2014; Taheri-Araghi et al., 2015; Si et al., 2019; Harris and Theriot, 2016). As the middle ground of these opposing views, it has been recently proposed that division is controlled concurrently by replication and growth-related processes; whichever of these processes completes the latest will trigger cell division (Micali et al., 2018a, 2018b; Colin et al., 2021).

Although the onset of constriction is one of the two critical cell-cycle checkpoints—the other being the initiation of replication—its timing relative to the replication cycle has not yet been determined in *E. coli* or other bacteria. Determining this timing based on images of cell shape is complicated because the change of cell width at the constriction region at the initial stages of septation is slow (Reshes et al., 2008). Since the experimental data have been missing, the existing cell-cycle models also do not consider the initiation of constriction as a cell-cycle checkpoint. Here, we use a new functional endogenous FtsN construct to determine the timing for the onset of constriction relative to the replication cycle. We use quantitative high-throughput fluorescence microscopy in microfluidic devices

to assess this timing in different growth rates and under genetic and chemical perturbations. Our experimental data and cell-cycle modeling are consistent with the idea that the replication cycle and the onset of constriction are coupled in slow growth conditions. The coupling weakens at faster growth rates. We then also investigate how this coupling is implemented at the molecular level. Our results suggest that the chromosome at the mid-cell blocks the onset of constriction via some form of nucleoid occlusion. However, a known nucleoid occlusion factor, SImA, is not the primary mediator for this regulation, and neither are the Ter linkage proteins. Our data thus imply that some additional molecular system implements nucleoid occlusion that affects the onset of constriction in *E. coli*. This nucleoid occlusion is lifted in a replication-dependent manner at approximately the time when replication terminates.

RESULTS

Timings for the onset of constriction and replication termination are highly correlated in slow growth conditions

To understand whether there is a coupling between replication and division cycles, we constructed *E. coli* strains in which fluorescent fusion proteins labeled both the replisome and the divisome (see Method details, Table S1). We used the N-terminal fusion of mCherry to DnaN (beta clamp) (Moolman et al., 2014) or the C-terminal fusion of Ypet to Ssb (single-strand binding protein) to label the replisome (Reyes-Lamothe et al., 2010). For the divisome label, we chose FtsN because it is the latest known component to assemble to the divisome, and its recruitment has been reported to coincide with the onset of constriction (Weiss, 2015; Liu et al., 2015; Haeusser and Margolin, 2016; Daley et al., 2016; Du and Lutkenhaus, 2019; Boes et al., 2019). While in previous fluorescent constructs of FtsN the labeled protein was expressed from extra copy plasmids (Liu et al., 2015; Soderstrom et al., 2018; Busiek and Margolin, 2014), in our construct, it was expressed from the native locus. We grew these strains in steady-state conditions in mother machine devices (Wang et al., 2010; Yang et al., 2018). The doubling times, T_d , and lengths of these cells were indistinguishable from the wild-type (WT) ones (strain BW27783) when grown in a glycerol medium (Table S3). Note that all of the measurements were performed at 28°C, where the growth rate is expected to be approximately 2 times slower than at 37°C (Herendeen et al., 1979). Using the fluorescently labeled strain, we followed the timing of replication termination (Trt), the onset of FtsN accumulation at mid-cell (Tn), and the onset of constriction (Tc) in time-lapse images (Figures 1A and 1B). Here, all of the times are given relative to cell birth. In addition, we determined the timing of replication initiation (Tri) and the replication period ($C = Trt - Tri$). We determined Tri , Trt , and Tn from the analysis of fluorescent images and Tc from the phase images (see Method details). We found Tc to be delayed relative to Tn on average by approximately 12 min (Figure S1). We assigned the delay to a less sensitive determination of constriction formation from phase images. We therefore use Tn instead of Tc for the timing of the constriction formation in the figures in the main text, while the data on Tc can be found in the figures in the supplemental information. We first investigated the correlation between termination and onset of constriction times in slow growth conditions in the M9 glycerol medium (Figure 1C). The Tn and Trt times were correlated (with a Pearson correlation coefficient $R = 0.94$)

as were the T_c and Trt times ($R = 0.92$; Figure S1). Comparable timings and correlations between T_c and Trt time were also present in a different strain, which carried the Ssb-Ypet label for replisome and no divisome label (Figure S2), indicating that Ypet fusion to FtsN and mCherry fusion to DnaN did not have significant effects on division and replication processes.

In 7% of cells, we found that the onset of constriction as measured by Ypet-FtsN (i.e., T_n) occurred before the termination (Trt) (Figure 1D). When we determined the onset of constriction from the phase images (T_c) in only 1 out of 420 cells termination occurred earlier than the onset of constriction (Figure S1), but as argued earlier, the latter estimate is likely less accurate. For 7% of cells, in which the initiation of constriction preceded the termination, the distribution of times $T_n - Trt$ was approximately exponential, with a characteristic time of 7 min (inset of Figure 1D). The latter time is close to the characteristic time that DnaN remains attached to the replication terminus region after the completion of replication (3 min at 37°C, potentially translating to approximately 6 min in our conditions) (Moolman et al., 2014). Altogether, the fraction of cells in which the termination of replication occurs after the actual onset of constriction is much smaller than 7%, if not zero. Interestingly, the distribution of $T_n - Trt$ was also approximately exponential for positive values, with a characteristic time of 15 min (Figure 1D and inset). The latter suggests that a single rate-limiting reaction may link the onset of constriction to the replication cycle.

We next investigated whether the above conclusions also applied at different growth rates. We repeated these measurements in an additional seven different growth media (Table S4); in three of these, the growth rates were slower, while in the other four, the rates were higher than in the measurement discussed above (Table S3). In all eight of these growth conditions, the average delay time $T_n - Trt$ was positive, meaning that on average, constriction formation follows the termination (Figure 2A and inset). $T_n - Trt$ showed variation between 20 and 40 min in different growth rates, except for the slowest growth rate in acetate medium where $T_n - Trt \approx 65$ min. Unlike the almost growth rate-independent behavior of $T_n - Trt$, the normalized delay times, $(T_n - Trt)/T_d$, showed two distinct growth-rate dependent regimes (Figure 2A). Below approximately $T_d \approx 130$ min, the normalized times decreased as the doubling time increased, but above it, the values plateaued, reaching approximately 12% of the cell cycle. A similar crossover from one regime to another was also seen in the Pearson correlation coefficients $R(T_n, Trt)$ (Figure 2B). For $T_d > 130$ min, the termination of replication and the onset of constriction were highly correlated ($R(T_n, Trt) > 0.85$) and independent of T_d , while for $T_d < 130$ min, these correlations decreased with the decreasing T_d . A similar crossover behavior could also be seen in plots when the timing of constriction (T_c) was determined from phase images (Figures S3A-S3E). The times of termination and constriction initiation were not only correlated but also followed a timer-like relationship, $T_n = Trt + \text{constant}$, at slower growth rates. This was evident in plots of Trt versus T_n , in which linear regression gave a slope of ≈ 1 for longer doubling times (Figure 2C). The corresponding intercept of the fits was almost independent of the doubling time (Figure S3E). Furthermore, we found that the distribution of delay times $T_n - Trt$ in a given growth condition was approximately exponential at slower growth rates, as it was for the growth condition described above (Figure S3F). This was also reflected in the coefficient of variation (CV) of these distributions, which was approximately one at longer doubling times

(Figure 2D). The CV values also showed a crossover at $Td \approx 130$ min. In shorter doubling times, the CV values decreased and the $Tn - Trt$ distributions shifted to positive values (Figure S3F). Altogether, the exponential distribution of delay times and the timer behavior in a range of slow growth conditions suggest a constant rate process linking the onset of constriction to the replication cycle. Irrespective of the details of this process, for $Td > 130$ min, our data are consistent with the idea that some replication-related process controls the initiation of constriction. However, as the doubling times shorten, this process becomes less and less rate limiting.

Modeling the coupling between the onset of constriction and the replication cycle in slow growth conditions

The presented data in slow growth conditions suggest that the onset of constriction is coupled to the replication cycle. However, the associated checkpoint may occur before the termination of replication. To narrow down the possible time range for this checkpoint, we constructed an analytical model. The model allows us to calculate the $Tn - Trt$ distributions and various statistics related to these distributions as a function of the timing of the checkpoint, Tx (Figure 3A). In the following discussion, we define the normalized time difference $x = (Trt' - Tx)/C$, namely the time delay between the true termination event, Trt' (as opposed to the measured termination event Trt) and the checkpoint Tx . In the above expression, C is the average C-period in a given growth condition, x ranges from 0 to 1, with $x = 0$ corresponding to a checkpoint at the termination and $x = 1$ to one at the initiation of replication. We furthermore assume that when the replication fork reaches a relative distance x from the replication terminus, the initiation of constriction occurs with a constant rate r (i.e., consistent with first-order reaction kinetics). The assumption of a single rate constant is based on the approximate exponential distribution for $Tn - Trt$ (for positive values) (Figures 1D and S3F), as well as the CV of this distribution being approximately equal to 1 (Figure 2D) in slow growth conditions. The model also accounts for the difference between the measured value of Trt and the actual one (Trt') due to the finite time that DnaN remains DNA bound after replication completes. The attachment time of DnaN to DNA, Ta , has been found to be exponentially distributed (Moolman et al., 2014). As discussed previously, a mean time of $Ta = 3$ to 6 min can be expected in our growth conditions. Under these assumptions, we find that the CV of the $Tn - Trt$ distribution is given by

$$CV(Tn - Trt) = \frac{\sqrt{\left(\frac{1}{r}\right)^2 + \sigma_C^2 x^2 + \langle Ta \rangle^2}}{\frac{1}{r} - \langle C \rangle x - \langle Ta \rangle}, \quad (\text{Equation 1})$$

(see Model coupling replication and constriction in Method details for the derivation). Here, σ_C is the standard deviation for the distribution of C-periods within the cell population. All of the quantities except x in Equation 1 (namely C , σ_C , r , and Ta) are determined from experiments (see Model coupling replication and constriction in Method details). We compared the predictions of the above formula to the measured CV values in the four slowest growth conditions. Equation 1 predicts that $CV(Tn - Trt)$ is close to 1 near $x = 0$ and rises rapidly with increasing x for all growth conditions considered (Figure 3B). The

experimentally measured CV values are thus consistent with the model only when x is close to zero—that is, when the constriction is initiated shortly before or at termination.

The Pearson correlation coefficients between Tn and Trt (Figure 3C) and the slopes of Tn versus Trt linear fits (Figure 3D), both of which can be derived analytically within the model, also show an agreement with the experimental data only when x is close to zero. In some growth conditions, however, the best agreement between model and data for the slope of Tn versus Trt occurs for larger values of x . The most outlying point in Figure 3D corresponds to mannose, where the data and the model agree at $x = 0.2$.

To further test the model, we also compared correlations and statistics between experimentally determined replication initiation, Tri , and constriction initiation, Tn , timings (Figures S4A-S4D; Table S5). We found that the model agrees with the experimental values of $CV(Tn - Tn)$ and $R(Tri, Tn)$ in all slow growth conditions for $x < 0.2$ (Figures S4E and S4F). In particular, the model predicts the slope of Tn versus Tri to be 1 for all values of x , which is indeed observed experimentally (Figure S4C). Altogether, the data and the model can be reconciled for the whole dataset if one assumes that the checkpoint is no more than $0.2C$ from the termination. It is important to emphasize that the agreement between the data and model can only be achieved for slow growth conditions ($Td > 130$ min). For faster growth rates, the model and the data do not agree for any value of x . This disagreement can be expected because the model assumes some replication-related process leading to the onset of constriction. As argued above, this assumption is not likely valid at faster growth rates.

Constriction can start before replication termination if the divisome is misplaced

Our goal was then to elucidate the molecular mechanism(s) that couple the onset of constriction to the replication cycle. Several molecular systems have been identified in the past that couple division and replication-related processes in *E. coli* (Männik and Bailey, 2015). These include the nucleoid occlusion factor SlmA (Bernhardt and de Boer, 2005); the Ter linkage proteins ZapA, ZapB, and MatP (Espeli et al., 2012; Bailey et al., 2014); and the DNA translocase FtsK (Sherratt et al., 2010). The first two of these systems have been implicated in the Z ring positioning relative to the replication terminus region of the chromosome, while FtsK can reposition misplaced chromosomes relative to the division plane at the end of constriction (Männik et al., 2017). We asked whether any of these systems are responsible for the correlated timing between replication termination and constriction initiation. We first considered the effects of SlmA, which is proposed to inhibit the formation of the Z ring before the Ter region of the chromosome moves to the center of the cell in a replication-dependent manner (Cho et al., 2011; Männik and Bailey, 2015). Its inhibitory effect is believed to be relieved from the mid-cell in the second half of the replication period because SlmA lacks binding sites at the Ter region. By removing SlmA from the cell, one would expect the formation of the Z ring and the constriction to start earlier. In contrast to this prediction, our data show that the $Tn - Trt$ period increased (Figure 4A) compared to the WT strain in slow growth conditions ($p = 2 \cdot 10^{-6}$, t test; Table S6). At the same time $R(Tn, Trt)$ decreased compared to WT but remained present at a significant level ($R = 0.7$; Figures 4B and S5). In previous work, CV has been used as a metric to identify whether a mutation in a particular protein has a significant effect on the

core regulatory process (Trueba et al., 1982; Soifer et al., 2016; Eun et al., 2018; Barber et al., 2020). If it does, then we would expect the CV to be enhanced, as the normalized distribution should become broader. However, we found change in $CV(Tn - Trt)$ in the *slmA* strain minor compared to WT (from 1.02 to 1.12; Figure S5E). The observations rule out that SlmA is the primary factor responsible for the timing of constriction formation. Rather, the above findings indicate that SlmA affects the timing of constriction indirectly, likely via its effect on the assembly of the Z ring.

Next, we investigated the role of the Ter linkage proteins ZapA, ZapB, and MatP. Unlike SlmA, which acts as an inhibitor, these proteins have been implicated in promoting the formation of the Z ring (Bailey et al., 2014). Together, ZapA, ZapB, and MatP form a proteinaceous chain that connects the replication terminus region of the chromosome to the Z ring. For this connection, all three proteins are needed (Espeli et al., 2012). Since these proteins promote Z ring formation, removing either ZapA, ZapB, or MatP from cells should delay Z ring formation and possibly the formation of the constriction. Indeed, removal of either of these three proteins increased $Tn - Trt$ in a statistically significant manner (Table S6), although the magnitude of the effect was small (less than 10% of cell-cycle time, <15 min) and the CV of the distributions was only moderately changed (Figure S5E). These observations indicate that the Ter linkage proteins, similar to SlmA, are unlikely to be directly involved in timing the constriction formation, and the observed effects likely arise via influences that the Ter linkage proteins have on the assembly of the Z ring.

We also investigated the role of FtsK, which is a late-arriving divisome component. FtsK has been implicated in segregating the replication terminus region at the onset of constriction (Stouf et al., 2013; Galli et al., 2017), although the segregation also occurs without active FtsK (Männik et al., 2017). One could expect the unsegregated terminus region to delay constriction closure. Using a translocation defective mutant FtsK K997A (Barre et al., 2000), we indeed found the $Tn - Trt$ time to increase. The observed effect was statistically significant (Table S6), although, again, still relatively small (11 min; 7% of cell-cycle time), including changes observed in $R(Trt, Tn)$ and $CV(Tn - Trt)$ (Figures 4B, S5D, and S5E). However, these data do not rule out the idea that the segregation of the replication terminus region is involved in regulating the onset of constriction. The small magnitude of the observed effect may be related to FtsK not being essential for the segregation of the Ter region. At the same time, the data do not support the idea that FtsK is part of the primary pathway that triggers the onset of constriction.

Although the Min system is not known to directly couple the replication and division processes, it is one of the main determinants for positioning the Z ring in *E. coli* (Männik and Bailey, 2015). In cells with a defective Min system, a fraction of divisions occurs close to the cell poles, while the remaining ones still occur in the vicinity of the middle of the cell. Distinguishing polar divisions from mid-cell divisions shows that polar divisions can start significantly earlier than the mid-cell ones (Figures 4C and 4D). Approximately half of the polar divisions started before replication had terminated. Furthermore $R(Trt, Tn) = 0.49$ was significantly lower than for other mutant strains or WT strains, and $CV(Tn - Trt) = -7.7$ was drastically altered (Figures S5D and S5E, respectively), indicating that some essential control mechanism for the onset of constriction was affected in these

divisions. At the same time, the timing of mid-cell divisions was instead slightly delayed (inset of Figure 4D), and $R(Trt, Tn)$ and $CV(Tn - Trt)$ effectively not affected compared to WT cells (Figures S5D and S5E). The findings related to polar divisions rule out the possibility that termination triggers constriction formation, as such a trigger would violate causality. However, a comparison of polar and mid-cell divisions raises the possibility that a replicating nucleoid in mid-cell can block constriction formation given that the division plane forms across the periphery of the nucleoid in polar divisions.

Nucleoid occlusion delays constriction formation in thymine-limited conditions

To further understand the coupling mechanism between replication and division cycles in slow growth conditions, we slowed down the replication period. To that end, we deleted *thyA* from our strain background and controlled the availability of thymine in the growth medium (Zaritsky et al., 2006). This strain had an indistinguishable C-period from the WT strain (approximately 90 min) when 500 $\mu\text{g/mL}$ thymine was present in the glycerol + trace elements media at 28°C. When thymine concentration was stepped down from 500 to 15 $\mu\text{g/mL}$, the C-period increased by approximately 40% to 125 min (Figure 5A). A step-like increase in the C-period in these cells was accompanied by transient increases in doubling times and in *Trt*, *Tni*, and *Tc* timings (Figure 5B). We verified that these transient increases were not a consequence of SOS-response caused by DNA damage by removing *sulA* and observing the same behavior (Figure S6A). We compared then the measured doubling times to predictions from the adder per the origin model (Ho and Amir, 2015) (Figure 5B), Cooper-Helmstetter (Cooper and Helmstetter, 1968; Wallden et al., 2016), the parallel adder (Logsdon et al., 2017; Witz et al., 2019), and the independent adder (Si et al., 2019) models (Figures S6B-S6D). The replication and division cycles are coupled in the first three models, while there is no coupling in the last one. The three models that include coupling between replication and division cycles qualitatively explained the data, while the independent adder model did not capture the transient increase in doubling times. The agreement between data and models was poorer at later times, in which all of the models predicted the doubling times to return to their original pre-step-down values, but the experimentally measured doubling times were approximately 10% longer. In these later times, thymine limitation is reported to affect beyond the replication speed, also the cell envelope biosynthesis (Rao and Kuzminov, 2020). Consistent with this idea, we observed membrane blebbing in some cells after long periods of thymine limitation. Notwithstanding the discrepancy at longer times, the models that postulate coupling between replication and division cycles can explain the transient increase in doubling times. In contrast, the model that lacks this coupling is qualitatively inconsistent with the data.

A closer examination of the transient period showed that the delay time $\langle Tn - Trt \rangle$ decreased after thymine step-down. It became temporarily negative at approximately 200 min after the step before increasing again (Figure 5C). At approximately 200 min after the thymine step, in approximately half of the dividing cell population, the onset of constriction occurred before termination of replication—that is, $Tn - Trt < 0$ (Figure 5C). In thymine-limited conditions, the onset of constriction can thus shift before the replication termination, although only for a short period (for approximately 50 min). This finding furthermore rules out that the termination of replication triggers the onset of constriction.

We then tested further the idea that a not-yet-fully replicated and segregated nucleoid in the mid-cell blocks the onset of constriction. To that end, we labeled nucleoids using HupA-mCherry and determined when the nucleoid density at the mid-cell started to decrease in the cell cycle, referring to this timing as T_{ng} (Figure S6E; see Method details). T_{ng} and the onset of constriction T_n timings showed high correlations ($R = 0.89$; Figure S6F) comparable to correlations between T_{rt} and T_n ($R = 0.94$, cf. Figure 1C). Also, the distribution of the delay times $T_n - T_{ng}$ (Figure S6G; $\langle T_n - T_{ng} \rangle = 18 \pm 23$ min) closely matched the distribution of $T_n - T_{rt}$ (Figure 1D; $\langle T_n - T_{rt} \rangle = 21 \pm 21$ min). The distribution had approximately exponential tails with characteristic times for negative values of $T_n - T_{ng}$ of 8 min and for positive values of 18 min. The minimum in nucleoid density thus appeared approximately at the same time as replication terminated. However, there are larger uncertainties in determining T_{ng} than T_{rt} stemming from the resolution of the microscope and the dynamic nature of the nucleoid.

We then determined how T_d , T_n , T_c , and T_{ng} from a strain with the same labels but a further deletion of *thyA* responded to the step-down in thymine (Figure 5D). Again, we observed a transient increase in doubling times and T_c , T_n , and T_{ng} timings. Unlike the average $\langle T_n - T_{rt} \rangle$, which becomes transiently negative, $\langle T_n - T_{ng} \rangle$ did not decrease under the thymine step-down (Figure 5C). The onset of constriction thus maintains its timing relative to the appearance of the local minimum in the nucleoid density at the middle of the cell, while the termination of replication does not. We also observed the same behavior for a strain that carried *slmA* deletion in addition to *thyA* (Figures S6H and S6I). Altogether, these findings are consistent with the idea that some form of nucleoid occlusion independent of SlmA controls the onset of constriction.

DISCUSSION

We found that the initiation of the constriction and the termination of the replication in *E. coli* were poorly correlated at fast growth rates, but the correlations increased as the growth rate slowed, reaching $R = 0.94$ for the slowest growth condition. The crossover from a correlated to an uncorrelated regime occurred at approximately $T_d \approx 130$ min, corresponding to $T_d \approx 65$ min at 37°C. A similar crossover appeared in $CV(T_n - T_{rt})$ and in the slope of T_{rt} versus T_n when plotted against T_d . Furthermore, the distributions of delay times $T_n - T_{rt}$ become approximately exponential for $T_d > 130$ min, suggesting that some replication-related process is rate limiting for the initiation of constriction.

One of our aims was to elaborate further on the coupling mechanism between replication and division cycles. The measurements with the *minC* deletion strain in slow growth conditions showed that in polar divisions, the initiation of constriction can precede the termination of replication, while the mid-cell divisions followed the same timings as in WT cells. This finding ruled out the possibility that termination acts as a trigger for constriction formation. Also, the finding ruled out that there can be a diffusible signal released at (Mulder and Woldringh, 1989) or before termination that triggers constriction formation. The diffusible signal should reach within seconds all cellular locations, including mid-cell and pole, and it will not lead to observable differences in the timing of constriction formation. Note that a protein synthesized in response to transcriptional activation is a

diffusible signal. The data thus rule out any possible mechanism in which the initiation of constriction is triggered in response to transcriptional activation of some gene. Instead of being triggered, the data from polar divisions suggested that a not-fully segregated chromosome in the mid-cell blocks constriction formation.

Further evidence that the nucleoid can block the onset of constriction formation comes from measurements in which we limited the availability of thymine for *thyA* cells. Thymine step-down increased the replication period by 40% in these conditions and led to a transient increase in doubling times. A transient increase in doubling times appears to have not been reported before despite the extensive use of thymine limitation to study the *E. coli* cell cycle (Zaritsky et al., 2006). The observed transient effect can only be explained if the replication and division cycles are coupled. The model in which these two cycles are uncoupled is qualitatively inconsistent with the data (cf. Figure S6D). At the same time, our data show that the delay times between the onset of constriction and replication termination became temporarily negative during this transient period. This finding furthermore rules out that the termination of replication is the trigger for the onset of constriction. However, the delay times between the onset of constriction (T_n) and the first detectable decrease in chromosomal DNA density at the mid-cell (T_{ng}) did not change throughout this transient period. This finding indicates that some form of nucleoid occlusion may be controlling division-related processes. The observed decrease in nucleoid density occurs on average at the termination in steady-state conditions. Furthermore, the distribution for $T_n - T_{ng}$ closely matches that of $T_n - T_{rt}$ at positive times, both being approximately exponential with a characteristic time of approximately 20 min. Based on the model in Figure 3A, this indicates that a single rate constant process links the onset of constriction and nucleoid segregation. The latter has, in turn, been driven by replication processes. However, it is as yet unclear in which exact event in the replication-segregation process the nucleoid occlusion is lifted. Modeling in Figure 3 shows that nucleoid occlusion may be lifted before the replication termination occurs. It is well established that daughter chromosomes segregate progressively as they are replicated (Nielsen et al., 2006; Youngren et al., 2014; Woldringh et al., 2015), although some rapid chromosomal movements also occur (Bates and Kleckner, 2005; Joshi et al., 2011). According to our data and modeling, lifting nucleoid occlusion may occur during some rapid changes in chromosomal conformation, called the snaps (Bates and Kleckner, 2005; Joshi et al., 2011), which have been observed before the two sister nucleoids separate from each other.

Nucleoid occlusion could also explain why DNA replication and division cycles are not coupled in fast-growth conditions. Indeed, as the growth rate increases in our measurements, the termination of the replication shifts earlier in the cell cycle (Figure S3G). In the fastest growth rates in the glucose-Cas medium, approximately half of the relevant terminations occur already in the mother cell. The latter means that approximately half of the cells in this growth condition are born with two nucleoids. These diploid cells have a nucleoid-free region at the mid-cell already at birth, and as a consequence, there is no blockage of the constriction by nucleoid at any point in the cell cycle. It has been largely overlooked that *E. coli* at faster growth rates can have two nucleoids at birth, although some support for this idea exists in previous studies (Männik et al., 2016; Si et al., 2019).

Although the coupling between the replication and division cycles appears to involve some form of nucleoid occlusion, it seems not directly related to the nucleoid occlusion factor SlmA. While the lack of SlmA or the Ter linkage proteins has a significant effect on the timing of the onset of constriction, these effects are small compared to the perturbations that occur during polar divisions. There could be some unknown nucleoid occlusion factor in *E. coli* that is not identified yet, as has been argued before (Cambridge et al., 2014; Rodrigues and Harry, 2012; Bailey et al., 2014; Bernard et al., 2010). These factor(s) could act at the level of FtsZ protofilament assembly or a later stage. It is also possible that there are no additional proteins involved, but the nucleoid occlusion arises directly from chromosome coils or transesterion linkages (Männik and Bailey, 2015), which present a steric hindrance for the formation and maturation of the Z ring. These possibilities should be examined in further studies. Altogether, our data indicate that some form of SlmA-independent nucleoid occlusion licenses division in a manner that depends on DNA replication and segregation. In slow growth conditions, this licensing is rate limiting for constriction formation. Our modeling studies suggest that the nucleoid occlusion is lifted within $0.2C$ from the termination (Figures 6A and 6B). Once the division is licensed, the constriction formation ensues via a constant rate process. At faster growth rates, some other competing process appears to become rate limiting (Figure 6C). The origin of the “other” process also remains to be determined. Some authors have proposed that the rate-limiting factors for the onset of constriction are precursor molecules for peptidoglycan synthesis (Harris and Theriot, 2016), such as lipid II. In contrast, others have concluded that it is the FtsZ protein (Si et al., 2019). Further work is thus needed to clarify the origin of this process.

The regulation proposed in Figure 6 is similar to the concurrent processes model (Micali et al., 2018a, 2018b; Colin et al., 2021), with some differences. First, the concurrent processes model does not consider the initiation of the constriction as a cell-cycle checkpoint. Instead, it predicts the timing and cell size at the division—that is, at the end of all division-related processes. It should be noted that all of the other current cell-cycle models in *E. coli* also predict only the end of the division. Second, in the concurrent processes model, replication and growth-related processes are both rate limiting for division in all growth conditions. Our data suggest that replication-related processes are rate limiting for constriction primarily in slow growth conditions, and the concurrency of the processes is only significant at the vicinity of the crossover region.

In conclusion, our work has shown that cell division is limited by replication-related processes in slow growth conditions but appears to be almost independent of these processes in faster growth rates in which some other processes become limiting. This behavior may explain why some earlier works have inferred that replication and division cycles are uncoupled from each other (Bernander and Nordstrom, 1990; Harris and Theriot, 2016; Si et al., 2019), while other authors have come to exactly opposite conclusions (Cooper and Helmstetter, 1968; Ho and Amir, 2015; Wallden et al., 2016; Witz et al., 2019). Our data furthermore imply that the limitation related to replication processes stems from some yet-to-be-identified form of nucleoid occlusion. This nucleoid occlusion is lifted in a replication-dependent manner at approximately the time when replication terminates. In addition to nucleoid occlusion, cells experience other types of licensing conditions that need

to be met. Whether all of these limiting processes couple to the divisome via the central hub of FtsZ protofilaments or other divisome components remains to be elucidated.

Limitations of the study

While we studied coordination between replication and division cycles over a range of different growth conditions, we could not determine the timing for termination, *Trt*, at fast growth rates. Our measurements in the EZ-Rich-defined medium showed too many overlapping foci of mCherry-DnaN, among which we were not able to distinguish individual initiation and termination events. The same problem on a lesser scale was also present in a glucose-Cas medium, in which we could not determine *Trt* in approximately 20% of correctly segmented cells (Figure S1E, see also Method details, Determination of *Trt* and *Tri* timings). With better image analysis tools to distinguish overlapping weak foci, one may overcome this shortcoming in the future.

Even though thymine limitation in *thyA* cells allows controllably to perturb the replication period, this limitation also perturbs other cellular processes such as the envelope biosynthesis (Rao and Kuzminov, 2020). These effects appear to dominate in the long-term response to thymine perturbation (beyond 400 min; Figure 5). One should be aware of these secondary effects when using thymine limitation as a tool to study the cell cycle.

STAR★METHODS

RESOURCE AVAILABILITY

Lead contact—Further information and requests for resources and reagents should be directed to the lead contact, Jaan Männik (JMannik@utk.edu).

Materials availability—All unique strains generated in this study will be available from the lead contact upon request.

Data and code availability—The experimental data used for Figures is available from Mendeley Data: <https://data.mendeley.com/datasets/hwzcywsc4/draft?a=d486eddf-c4c6-40ee-b262-913f79e5d47b>. <https://doi.org/10.17632/hwzcywsc4.1>.

The code used in modeling can be found in GitHub:<https://github.com/pkar96/Coupling-between-DNA-replication-segregation-and-the-onset-of-constriction-in-Escherichia-coli>.

Any additional information required to reanalyze the data reported in this paper is available from the lead contact upon request.

EXPERIMENTAL MODEL AND SUBJECT DETAILS

Bacterial cells—We used *E. coli* BW27783 cells in our studies, which are derivatives of K-12 strain. The cells were cultured in defined M9 media at 28°C.

METHOD DETAILS

Construction of *E. coli* strains—All *E. coli* strains used in the reported experiments are derivatives of K12 BW27783 obtained from the Yale Coli Genetic Stock Center (CGSC#:

12119). STK13 strain (*ftsN::frt-Ypet-ftsN*, *dnaN::frt-mCherry-dnaN*) was constructed by λ -Red engineering (Datsenko and Wanner, 2000) and by P1 transduction. For chromosomal replacement of *ftsN* with fluorescence derivative, we used primers carrying 40nt tails with identical sequence to the *ftsN* chromosomal locus (see Key resources table) and a plasmid carrying a copy of Ypet preceded by a kanamycin resistance cassette flanked by *frt* sites (*frt-Kan^R-frt-Ypet-linker* sequence SAGSAAGSGSA) as PCR template (a kind gift from R. Reyes-Lamothe (Reyes-Lamothe et al., 2010)). The resulting PCR product was transformed by electroporation into a strain carrying the λ -Red-expressing plasmid pKD46. Colonies were selected by kanamycin resistance, verified by fluorescence microscopy and by PCR using primers annealing to regions flanking *ftsN* gene. After removing kanamycin resistance by expressing the Flp recombinase from plasmid pCP20 (Cherepanov and Wackernagel, 1995), the mCherry-*dnaN* gene fusion (BN1682 strain; a kind gift from N. Dekker (Moolman et al., 2014)) was transferred into the strain by P1 transduction. To minimize the effect of the insertion on the gene expression levels, the kanamycin cassette was removed using plasmid pCP20. Specific gene mutations (e.g. single gene deletions of Keio collection (Baba et al., 2006) and FtsK^{K997A} (Kennedy et al., 2008) were introduced into the STK13 strain by P1 transduction (see Table S1).

For thymine-limitation experiments, both *thyA* and *sulA* deletion strains were created by λ -Red engineering in a BW25113 (CGSC#:7636) background. For *thy* strain, Kan^R sequence from pROD62 plasmid (a kind gift from R. Reyes-Lamothe) and for *sulA*, *frt-CM^R-frt* sequence from pKD32 plasmid (CGSC#: 7988) was used as a PCR template. Further, these mutations were introduced into the STK13 strain by P1 transduction to create STK37 and STK39 strains. For nucleoid DNA density visualization, strain STK46 was created by P1 transduction of HupA-mCherry (a kind gift from P. Bissichia and D. Sherratt) into the strain with Ypet-FtsN label. Detailed information on strain genotypes and construction information is listed in Table S1. Oligonucleotide information is given in Table S2. For *E. coli* strain engineering, cells were grown in lysogeny broth (LB) and appropriate selective antibiotics.

Growth media and growth conditions—For time-lapse imaging in microfluidic devices, cells were cultured in 8 different growth conditions at 28°C. Detailed information on the media used can be found in Table S4.

Cell preparation and culture in microfluidic devices—All bacterial strains were streaked on agar plates containing M9 minimal salts supplemented with 2 mM magnesium sulfate, corresponding carbon sources, and appropriate selective antibiotics. A day before an experiment a less than 10 days old colony was inoculated into 3 mL of M9 minimal salts media (Teknova Inc., CA) supplemented with corresponding carbon sources, trace metals mixture (Teknova Inc., CA, #T1001), casamino acids (ACROS Organics) and appropriate antibiotics when needed. Unless otherwise indicated, antibiotics were used at 25 μ g/mL of kanamycin (Kan) and 25 μ g/mL chloramphenicol (CM). For microscopy experiments, cells were grown to an OD₆₀₀ of ~0.1 in a liquid medium and then concentrated ~100x by centrifugation in the presence of 75 μ g/mL of BSA (Bovine Serum Albumin; Millipore Sigma, MO) to minimize clumping of the cells. The resulting solution was

used to inoculate microfluidic mother machine devices. The latter were made of PDMS (polydimethylsiloxane) following a previously described procedure (Yang et al., 2018). For inoculation 2–3 μL of resuspended concentrated culture was pipetted into the main flow channel of the device. The cells were then let to populate the dead-end channels. Once these channels were sufficiently populated (about 1 h), tubing was connected to the device, and the flow of fresh M9 medium with corresponding carbon sources and supplements, and BSA (75 $\mu\text{g}/\text{mL}$) was started. The flow was maintained by a NE-1000 Syringe Pump (New Era Pump Systems, NY) at 5 $\mu\text{L}/\text{min}$ during the entire experiment. To ensure steady-state growth, the cells were left to grow in channels at least 14 h (24 h for acetate) before imaging started. We used the same conditions as above for thymine step-down experiments, except that in addition to regular M9 media with 500 $\mu\text{g}/\text{mL}$ of a thymine-containing syringe, the second syringe pump for low thymine concentration (15 $\mu\text{g}/\text{mL}$; Table S4) was connected to the device. Before applying thymine step-down, cells were imaged in the regular growth media. After imaging for approximately 4 generation times, the first pump with the regular growth media was turned off, and the second syringe pump containing the low thymine media was turned on during imaging using a custom-made LabVIEW program.

Fluorescence microscopy—A Nikon Ti-E inverted fluorescence microscope (Nikon Instruments, Japan) with a 100X NA 1.40 oil immersion phase contrast objective (Nikon Instruments, Japan) was used for imaging the bacteria. Images were captured on an iXon DU897 EMCCD camera (Andor Technology, Ireland) and recorded using NIS-Elements software (Nikon Instruments, Japan). Fluorophores were excited by a 200W Hg lamp through ND4 and ND8 neutral density filters. Chroma 41004 and 41001 filter cubes (Chroma Technology Corp., VT) were used to record mCherry and Ypet images, respectively. A motorized stage (Prior Scientific Inc., MA) and a Nikon Perfect Focus $\text{\textcircled{R}}$ system were utilized throughout time-lapse imaging.

Image analysis—MATLAB, along with the Image Analysis Toolbox and DipImage Toolbox (<http://www.diplib.org/>) were used for all image analyses steps detailed below. In all analyses of time-lapse recordings, corrections to subpixel shifts between different frames were applied first. These shifts were determined by correlating phase-contrast images in adjacent frames. The cells were then segmented based on phase-contrast images using a custom MATLAB script. Timings of cell divisions were corrected based on the dissociation of the Ypet-FtsN label from the septum in strains where this label was present. Timings of replication initiation and termination, and initiation of constriction were determined from corresponding time-lapse images. For the Figures in the main text the replication initiation, T_{ri} , and termination, T_{rt} , timings were determined from the time-lapse images of the mCherry-DnaN label (strain STK13), for the detailed procedures, see below. In glycerol and glucose-Cas growth media, these timings were also determined using a different strain (JM85), which expressed the Ssb-Ypet label. The data from the latter strain are shown in SI Figures.

Determination of T_n timing—The timing for the onset of constriction, T_n , was determined based on the appearance of the Ypet-FtsN signal at midcell via a semiautomated and a fully automated approach. For the semiautomated analysis, the intensity line profiles

along the long axes of the cell from each time point were collected to a kymograph such as shown in Figure 1B, middle. The intensity of these profiles could be scaled during the analysis. The earliest detectable increase in Ypet-FtsN intensity above the background level was marked, and the corresponding timing was used as T_n . This timing is plotted in all Figures. To verify the lack of bias in these estimates, we used a fully automated analysis. In the fully automated analysis, the intensity line profiles from each frame were fitted to a Gaussian distribution with a constant background. If the fitted peak contained more than 5% of the total fluorescence signal from the cell, the FWHM of the Gaussian was between about 200 and 1000 nm, and the peak was not more than 10% off from the cell center in terms of cell length then this fitting qualified as an FtsN accumulation. These accumulations were further filtered to extract a single cluster of accumulations in each cell cycle. In this filtering, the presence of accumulations was tracked from the division frame towards the birth frame. If an accumulation was missing in one frame but present in at least two previous frames, then the lack of this accumulation was ignored. Otherwise, tracking of the accumulations stopped, and the timing of the earliest accumulation present in the tracked set of points was assigned to T_n . Both methods yielded T_n distributions whose means were not significantly different (t test, $p > 0.05$).

Determination of T_c timing—In an alternative way, the onset of constriction, T_c , was determined from the phase images. The intensity line profiles from the segmented phase-contrast images were collected to kymographs as described above. After scaling the intensities, the earliest detectable increase in the phase signal at the midcell was marked as T_c (cf. Figure 1B, bottom). This determination of T_c was further verified by plotting phase intensities collected from the about 1 μm wide band in the midcell as a function of time. In the latter analysis, the start of a steady increase of the midcell phase signal from a slowly varying baseline at the early cell cycle stages was marked as T_c . The typical variation of the intensity at the baseline level was about 5%. This variation limited the accuracy by which T_c could be detected.

Determination of T_{rt} and T_{ri} timings—To detect T_{rt} and T_{ri} timings, kymographs of mCherry-DnaN or Ssb-Ypet intensity line profiles were compiled. T_{ri} and T_{rt} were determined as the beginning and the end of the midcell accumulation of the fluorescent maker, respectively (Figure 1B, top). Consistent with the earlier works (Reyes-Lamothe et al., 2008), occasionally, a single focus of mCherry-DnaN or Ssb-Ypet split to two foci in this band. The splitted focus was still considered to be part of the continuous midcell band. This initial analysis was verified in the following way. First, fluorescence intensity line profiles were fit independently by a second-order polynomial corresponding to the background, a single Gaussian peak, or two Gaussian peaks. The chi-square value of each of these three fits was determined, and the corresponding probability from the cumulative chi-square distribution was calculated. This probability reflects the chance that random fluctuations in the data could have given rise to the corresponding model. Of the three fits, the one with the lowest probability was selected. If the lowest probability distribution corresponded to a second-degree polynomial, then this indicated lack of ongoing replication. In other cases, ongoing replication was considered to be present. Next, the total fluorescence intensity was plotted as a function time, either within a single or two Gaussian peaks. This total intensity

abruptly increased at the beginning of the replication (Tri) and decreased at the end (Trt). These abrupt changes were marked as Tri and Trt timings.

In faster growth conditions, terminations can occur either in the early or late stages of the cell cycle. Considering the terminations only in the cell cycle when the division occurs will give a bimodal distribution of Trt times. However, the late terminations in the cell cycle could not be relevant for the onset of division because they mostly occurred after the onset of constriction. We, therefore, did not consider these late terminations but instead recorded terminations that occurred in mother cells. This approach yielded a continuous unimodal distribution of Trt times for cell population in a given growth condition. In this distribution, the Trt times are negative if termination occurs in the mother cell. $Trt < 0$ also indicated that the daughter cell was born with two distinct chromosomes. Note also that the two terminations in the mother cell were not always precisely synchronous. For a given cell of interest, we determined the timing of the termination for the chromosome that was inherited by this cell. In the fastest reported growth condition in M9 glucose-Cas medium, we could not determine Trt in about 20% of correctly segmented cells. Unlike in other reported growth conditions, there appeared no delay between the termination and the next round of initiation in these cells (Figure S1E). These cells were left out from the further analysis.

Similar to the termination, the relevant initiations of replication could occur in the mother cell. In M9 glucose-Cas media, the relevant initiations mostly occur in the mother cells but also in the grandmother cells. We could not determine these initiations unambiguously. We, therefore, do not report Tri in M9 glucose-Cas media. In other growth media, the initiation occurred either in the mother cell or in the cell of interest. If the initiation occurred in the mother cell, then the initiation of the chromosome inherited by the cell of interest was used. The time difference between the two initiations in the mother cell was typically within 8 min interval.

Determination of Tng timing—For determining the timing of the nucleoid density decrease at the midcell (Tng), nucleoids were visualized using the nucleoid-associated protein HU, fluorescently tagged via its HupA subunit (HupA-mCherry), which has been shown to label bacterial DNA similar to DAPI labeling (Wery et al., 2001). In a fully automated analysis, the intensity line profile along the long axis of the cell from the HupA-mCherry signal was first found. This signal was inverted and normalized by maximum signal intensity. Next, all the local maxima/peaks in this signal were determined. Then only peaks that were no more than 0.4 μm from the middle of the cell and at least 0.05 high in normalized units from their surrounding (0.4 μm away) were retained. If filtered peaks were not detected in two or more consecutive frames starting from the division frame, then that last detected frame of a filtered peak determined the Tng for that cell. The chosen threshold (0.05) produced the closest match to the same timings that we determined manually by inspecting minima in intensity line traces of HupA-mCherry signal (Figure S6E). Lowering the threshold caused Tng times to become smaller and raising it caused the times to increase, but these shifts did not change the overall shape of $Tng(t)$ curves in thymine step-down experiments.

QUANTIFICATION AND STATISTICAL ANALYSIS

Different distributions of $T_n - Trt$ times were compared using two-tailed unpaired t test. The Matlab function *ttest2* was used for testing. Error bars for the Pearson R-values represent 95% confidence intervals. These intervals were calculated using Fisher's z-transformation (Nicholls, 2014). Briefly, based on the measured R-value the corresponding z-value was calculated as $z = 1/2 \ln(1 + R/(1 - R))$. The 95% confidence intervals for z were calculated as $z_{CI} = [z - 1.96 / \sqrt{N - 3}, z + 1.96 / \sqrt{N - 3}]$ where N is number of measurements for a given R-value. Number of cells analyzed (N) in different measurements is listed in Table S3. The intervals were then backtransformed for R confidence intervals using $R_{CI} = (\exp(2z_{CI}) - 1) / (\exp(2z_{CI}) + 1)$. Error bars for the coefficient of variation (CV) also represent 95% confidence intervals. These intervals were determined by bootstrapping. Bootstrapping was carried out in Python 3.7. by sampling the distributions 10^4 times and verifying that the resulting CV distributions did not change upon further doubling the samples. Percentile intervals were found using *numpy percentile* method.

Model coupling replication and constriction—We assume that cells initiate DNA replication at time Tri and that nucleotides are added to the growing strand of DNA at a constant rate γ . We denote the length of the *E. coli* genome (measured in nucleotide number) as N . Using the central limit theorem, the time taken to reach termination (the C-period) is normally distributed with a mean $\frac{N}{\gamma}$ and variance $\frac{N}{\gamma^2}$. The CV of the C period thus scales as $\frac{1}{\sqrt{N}}$ with $N \approx 4 \cdot 10^6$. Thus, the predicted CV is two orders of magnitude smaller than that experimentally observed (Table S5), and we conclude that the variability in the C period resulting from stochastic nucleotide addition is negligible. Hence, we can consider the replication process to be happening at a constant velocity v . The time taken for replication to complete is then given by $\frac{N}{v}$, and variability in the C period results from the cell-to-cell variability in v .

Experimentally, the C-period and Td are strongly and positively correlated (Table S5). This would suggest that the progress of biochemical processes like DNA replication scales with the individual growth rate of the cells. In this case, a slower-growing cell will also replicate at a slower velocity and subsequently have a longer C period. The scaling with growth rate points to a small but non-negligible variability in v within the population of growing cells in a particular media.

Since C is assumed uncorrelated with the initiation time, the time at termination Trt' is thus:

$$Trt' = Tri + C. \quad (\text{Equation 1})$$

The evidence for such a “timer” can be found in Table S5, which lists the slope of linear regression for Trt vs Tri plots in different growth conditions. As can be seen from Table S5, this slope is close to one in slow growth conditions.

In the experiments, the replisome is imaged using a DnaN marker. The DnaN marker is expected to remain attached to the replication terminus region after completion of replication (Moolman et al., 2014). Thus, in experiments the measured time of termination Trt is,

$$Trt = Trt' + Ta, \quad (\text{Equation 2})$$

where Ta is the time for which DnaN stays attached. Ta is assumed to be exponentially distributed with a mean time $\langle Ta \rangle = 3\text{--}6$ min expected in our growth conditions (Moolman et al., 2014).

We assume Tri to be normally distributed with mean $\langle Tri \rangle$ and standard deviation σ_{Tri} , the values for which are determined from experiments. Assuming v to be normally distributed with a mean v_0 and standard deviation σ_v , the C period has an approximately normal distribution with mean $\langle C \rangle = \frac{N}{v_0}$ and variance $\sigma_C^2 = \left(\frac{N\sigma_v}{v_0}\right)^2$ when $\sigma_v \ll v_0$. Using Equations 1 and 2, we can determine $\langle C \rangle$ and σ_C^2 to be,

$$\langle C \rangle = \langle Trt - Tri \rangle - \langle Ta \rangle, \quad (\text{Equation 3})$$

$$\sigma_C^2 = Var(Trt - Tri) - \langle Ta \rangle^2. \quad (\text{Equation 4})$$

$\langle Trt - Tri \rangle$ and $Var(Trt - Tri)$ are the mean and variance of $Trt - Tri$ and are determined directly from experiments (Table S5).

In our model, constriction is said to be controlled by an event placed at a locus that is a relative distance of x from the replication terminus. $x = 0$ denotes the locus is at the terminus while $x = 1$ denotes a checkpoint at the initiation. Under the assumption that v has a Gaussian distribution with $CV \ll 1$, we obtain that the checkpoint is triggered after a time ξ from initiation which is normally distributed with mean $\langle C \rangle(1 - x) = \frac{N(1 - x)}{v_0}$ and variance $\sigma_C^2(1 - x)^2 = \left(\frac{N(1 - x)\sigma_v}{v_0}\right)^2$. Thus, the checkpoint is said to be reached at time Tx given by,

$$Tx = Tri + \xi. \quad (\text{Equation 5})$$

Since termination happens at a fraction x along the genome from Tx ,

$$Trt' = Tx + \zeta, \quad (\text{Equation 6})$$

where ζ is normally distributed with mean $\langle C \rangle x$ and variance $\sigma_C^2 x^2$. Note that ξ and ζ are correlated with each other with covariance $Cov(\xi, \zeta) = \sigma_C^2 x(1 - x)$. Both ξ and ζ are also correlated with the C period.

Constriction is assumed to be triggered by the checkpoint at time Tx at a constant rate r . This is based on the fact that the positive values of $Tn - Trt$ are exponentially distributed

(Figure 1D) and the CV of $Tn - Trt$ is close to one (Figure 2D). Hence, the time at constriction Tn is,

$$Tn = Tx + Txn. \quad (\text{Equation 7})$$

Txn is exponentially distributed with a mean time = $\frac{1}{r}$. Using Equations 2 and 6, we get

$$\frac{1}{r} = \langle Tn - Trt \rangle + \langle Ta \rangle + \langle C \rangle x. \quad (\text{Equation 8})$$

$\langle Tn - Trt \rangle$ can be determined from experiments thus fixing the rate r for different x . x is a free parameter whose value is yet to be determined. Using the experimental results plotted in Figure 2 and comparing them against the analytical results for varying x , we obtain constraints on the value of x .

We shall first calculate analytically $CV(Tn - Trt)$ for a given value of x , which can be compared to experimentally determined values shown in Figure 2D. Using Equations 2, 6 and 7, we get,

$$Tn - Trt = Txn - (\zeta + Ta). \quad (\text{Equation 9})$$

Txn , ζ , Ta are independent of each other. Hence the variance of $Tn - Trt$ is

$$Var(Tn - Trt) = \left(\frac{1}{r}\right)^2 + \sigma_C^2 x^2 + \langle Ta \rangle^2, \quad (\text{Equation 10})$$

while the mean is $\frac{1}{r} - (\langle C \rangle x + \langle Ta \rangle)$. Combining the two, we find:

$$CV(Tn - Trt) = \frac{\sqrt{\left(\frac{1}{r}\right)^2 + \sigma_C^2 \cdot x^2 + \langle Ta \rangle^2}}{\frac{1}{r} - \langle C \rangle x - \langle Ta \rangle}. \quad (\text{Equation 11})$$

Other statistical constructs presented in Figure 2 include the Pearson correlation coefficient for Trt , Tn , $R(Tn, Trt)$ and the slope of linear regression for Tn vs Trt plot.

$R(Tn, Trt)$ is defined as,

$$R(Tn, Trt) = \frac{\langle (Tn - \langle Tn \rangle)(Trt - \langle Trt \rangle) \rangle}{\sigma_{Trt} \sigma_n}, \quad (\text{Equation 12})$$

where σ_{Trt} and σ_n are the standard deviations of Trt and Tn , respectively.

From Equations 5 and 7, we obtain $Tn = Tri + Txn + \xi$. Similarly, from Equations 1 and 2, $Trt = Tri + C + Ta$. All pairs of variables from Tri , C , Ta , Txn , ξ are uncorrelated with each other except C and ξ which are correlated as remarked earlier. Substituting this into Equation 12, we find the covariance (numerator) to be,

$$\langle (Tn - \langle Tn \rangle)(Trt - \langle Trt \rangle) \rangle = \langle Tri^2 \rangle - \langle Tri \rangle^2 + \langle C\xi \rangle - \langle C \rangle \langle \xi \rangle = \sigma_{ri}^2 + \sigma_C^2(1-x). \quad (\text{Equation 13})$$

σ_n and σ_{rt} are found to be:

$$\sigma_n^2 = \sigma_{ri}^2 + \left(\frac{1}{r}\right)^2 + \sigma_C^2(1-x)^2, \quad (\text{Equation 14})$$

$$\sigma_{rt}^2 = \sigma_{ri}^2 + \sigma_C^2 + \langle Ta \rangle^2. \quad (\text{Equation 15})$$

Substituting Equations 13, 14, and 15 into Equation 12, we can obtain $R(Tn, Trt)$. All the parameters in the formula for $R(Tn, Trt)$ can be extracted from experiments while x is a variable.

The slope of the linear regression line for Tn vs Trt is related to $R(Tn, Trt)$ as

$$\text{Slope}(Tn, Trt) = \frac{R(Tn, Trt)\sigma_n}{\sigma_{rt}}. \quad (\text{Equation 16})$$

This can also be calculated by substituting the values in Equations 13, 14, and 15. This theoretical prediction is compared to the experimental data in Figure 2C.

Assuming the trigger for the constriction event to be at termination (i.e., $x = 0$), we can obtain the distribution of $Tn - Trt$ times analytically and compare it to experimental distributions. For $x = 0$, we obtain $Tn - Trt = Txn - Ta$. Let us define the random variable $Z = Tn - Trt$. We aim to find its distribution. Using our assumptions that Txn and Ta are independent and exponentially distributed, we obtain the joint probability distribution of Txn and Ta to be,

$$f(t_{xn}, t_a) = \frac{r}{\langle Tr \rangle} e^{-rt_{xn}} \cdot e^{-\frac{t_a}{\langle Ta \rangle}}. \quad (\text{Equation 17})$$

For $z \geq 0$,

$$P_+(Z \leq z) = \frac{r}{\langle Ta \rangle} \int_0^\infty e^{-\frac{t_a}{\langle Ta \rangle}} dt_a \int_0^{t_a+z} e^{-rt_{xn}} dt_{xn} = 1 - \frac{e^{-rz}}{1+r\langle Ta \rangle}, \quad (\text{Equation 18})$$

with $P_+(Z \leq z)$ the cumulative distribution function (CDF) of Z for $z \geq 0$. Similarly, for $z < 0$, we obtain,

$$P_{-}(Z \leq z) = \frac{r}{\langle Ta \rangle} \int_{-z}^{\infty} e^{-\frac{t_a}{\langle Ta \rangle}} dt_a \int_0^{t_a+z} e^{-rt_{xn}} dt_{xn} = \frac{r\langle Ta \rangle}{1+r\langle Ta \rangle} e^{-\frac{z}{\langle Ta \rangle}}. \quad (\text{Equation 19})$$

Therefore, we find that the probability distribution of $Z = Tn - Tri$, $g(z) = \frac{dP(z)}{dz}$ is

$$g(z) = \frac{1}{\frac{1}{r} + \langle Ta \rangle} \begin{cases} e^{-rz}, & z \geq 0 \\ e^{-\frac{z}{\langle Ta \rangle}}, & z < 0 \end{cases}. \quad (\text{Equation 20})$$

The parameters can be determined using the experimental data as discussed before.

Finally, we also investigate the relationship between replication initiation timing Tri and timing for initiation of constriction Tn . As before we will calculate the relevant statistics as a function of x . We will rely on the fact that $Tn = Tri + Txn + \xi$, and that Tri , Txn and ξ are uncorrelated. The variance of $Tn - Tri$ is found to be,

$$Var(Tn - Tri) = \left(\frac{1}{r}\right)^2 + \sigma_C^2 (1-x)^2, \quad (\text{Equation 21})$$

while the mean of $Tn - Tri = \frac{1}{r} + \langle C \rangle (1-x)$. Thus, $CV(Tn - Tri)$ is found to be,

$$CV(Tn - Tri) = \frac{\sqrt{\left(\frac{1}{r}\right)^2 + \sigma_C^2 (1-x)^2}}{\frac{1}{r} + \langle C \rangle (1-x)}. \quad (\text{Equation 22})$$

Other statistical constructs which we calculate include the Pearson correlation coefficient for Tri , Tn , $R(Tn, Tri)$ and the slope of linear regression for Tn vs Tri plot.

$R(Tn, Tri)$ is defined as,

$$R(Tn, Tri) = \frac{\langle (Tn - \langle Tn \rangle)(Tri - \langle Tri \rangle) \rangle}{\sigma_{ri} \sigma_n}, \quad (\text{Equation 23})$$

Using $Tn = Tri + Txn + \xi$, we find the numerator to be:

$$\langle (Tn - \langle Tn \rangle)(Tri - \langle Tri \rangle) \rangle = \sigma_{ri}^2. \quad (\text{Equation 24})$$

The quantity σ_{ri} is directly inferred from experiments while σ_n is calculated using Equation 14. Substituting the values into Equation 23, we can obtain $R(Tn, Tri)$. The slope of the linear regression line between Tn and Tri is related to $R(Tn, Tri)$ as

$$\text{Slope}(T_n, T_{ri}) = \frac{R(T_n, T_{ri})\sigma_n}{\sigma_{ri}} = 1. \quad (\text{Equation 25})$$

Hence, the slope of the linear regression line for T_n vs T_{ri} is always one independent of growth conditions. In other words, within the model T_n is related to T_{ri} via a timer. In the four slowest growing conditions, the slope between T_n vs T_{ri} is indeed close to 1 as shown in Figure S4C.

MODELING OF THYMINE SHIFT EXPERIMENTS

To test whether the transient increases in doubling times T_d in thymine step-down measurements can be explained by coupling between the replication and division cycles, we performed simulations of different cell cycle models:

1. Cooper Helmstetter (CH) model (Cooper and Helmstetter, 1968; Wallden et al., 2016)
2. Adder per origin (AO) model (Ho and Amir, 2015)
3. Parallel adder (PA) model (Logsdon et al., 2017; Witz et al., 2019)
4. Independent adder (IA) model (Si et al., 2019)

In CH, AO, and PA models, the replication and division cycles are coupled while they are uncoupled in the IA model.

For the simulations of all models, the initial condition is that all cells are born and initiate DNA replication at the beginning of the simulation. The time is thereafter incremented by 0.01 min intervals. In each time increment, the cells grow exponentially in size with the growth rate fixed within a cell cycle. On division, the growth rate for that cell cycle is drawn from a normal distribution with mean $\langle \lambda \rangle$ and coefficient of variation (CV_λ). The number of origins is also tracked throughout the simulations beginning with an initial value of 2. Cells divide into two daughter cells in a perfectly symmetrical manner (no noise in division ratio) and both the daughter cells are tracked for roughly five generations (time $t = 5 \langle T_d \rangle$) to ensure that a steady-state has been reached. From time $t > 5 \langle T_d \rangle$ onwards, only one of the daughter cells is tracked to mimic the mother-machine experiment. The thymine step-down occurs at time $t = 7 \langle T_d \rangle$ leading to changes in simulation parameters.

For the plots of variation of T_d with time, the time corresponds to the difference between the time at which the cell divides and the time at which the thymine step-down occurs i.e., cells dividing prior to the thymine shift-down correspond to time < 0 . The simulations are iterated 300 times with the same initial conditions, and the results shown correspond to the mean binned data (Figures 5B, 5D and S6) over the 300 iterations.

Parameters of the model—All model parameters are obtained from the experiments conducted on *thyA* (STK37) strain. Cells which divide within time = 100 min from the thymine step-down (corresponds to cells in the time range -100 min– 0 min) are considered

for fixing parameter values. The time range is picked as such to ensure that cells are in steady state.

Growth rate—The mean growth rate is set to $\frac{\ln(2)}{\langle Td \rangle}$ and CV_λ is equal to the CV of the quantity, $\frac{1}{Td} \ln\left(\frac{Ld}{Lb}\right)$, where Lb is the length at birth and Ld is the length at the division.

Length at initiation—For the AO, PA and IA models, the length at initiation is given by an adder per origin between successive initiation of DNA replication. Thus, the total length ($L_i^{tot,next}$) at which the next initiation happens is determined by the length at initiation (L_i) in the current cell cycle by,

$$L_i^{tot,next} = L_i + O \Delta_{ii}, \quad (\text{Equation 1})$$

where Δ_{ii} is the length added per origin, and O is the number of origins. Δ_{ii} is drawn from a normal distribution with a mean $\langle \Delta_{ii} \rangle$ and standard deviation $\sigma_{\Delta_{ii}}$. The values of $\langle \Delta_{ii} \rangle$ and $\sigma_{\Delta_{ii}}$ are set equal to the experimentally measured values of $\frac{\langle Li \rangle}{2}$ and $\frac{\sqrt{3}\sigma_i}{2}$, respectively, where $\langle Li \rangle$ is the mean and σ_i is the standard deviation of L_i obtained from experiments.

For the CH model, the length at initiation is determined by a sizer at the initiation. When the cell reaches a critical size per origin the cell divides. The critical size per origin at initiation for each cell cycle is drawn from a normal distribution with the average fixed using the experimentally measured value of $\frac{\langle Li \rangle}{2}$ and standard deviation being equal to $\frac{\sigma_i}{2}$.

Length at division—The length at division is determined by the specific model being simulated.

For the AO and CH model, division happens after a duration $C + D$ from initiation. Thus, the length at division, Ld is,

$$Ld = L_i e^{\lambda(C+D)}, \quad (\text{Equation 2})$$

$C + D$ is drawn from a normal distribution on reaching the initiation length and the time obtained determines when the corresponding division occurs. The mean and standard deviation of $C + D$ is set to match that obtained from experiments. After the thymine shift, the C -period is found to increase in the experiments, as expected. For the AO and CH models, this corresponds to an increase in the mean of the $C + D$ period. So, in the simulations, the $C + D$ time is drawn from a normal distribution with a mean greater by ~ 40 min after the thymine shift as compared to before the shift.

For the PA model, initiation and division are linked via an adder, as shown in Equation 3. Scaling by the number of origins (O) rectifies for extra initiations within a cell cycle.

$$Ld = L_i + O \Delta_{id}, \quad (\text{Equation 3})$$

where id is the length added between initiation and division per origin.

In the simulations, once initiation length is reached, id is drawn from a normal distribution with the same mean and CV as that of experiments and the division length is set by Equation 3. After the thymine shift, the model parameter id is increased by $0.22 \mu\text{m}$ as determined experimentally.

For the IA model, the length at division is determined by the length at birth via an adder mechanism, independent of the replication cycle. The division length is set to be,

$$Ld = Lb + \Delta_{bd} . \quad (\text{Equation 4})$$

In the simulations, at the start of each cell cycle, bd is drawn from a normal distribution with mean and CV identical to the experiments. After the thymine shift, there is no change in parameters as the C-period is not a relevant model parameter in this case.

Supplementary Material

Refer to Web version on PubMed Central for supplementary material.

ACKNOWLEDGMENTS

The authors thank Ethan Garner, Conrad Woldringh, and Arieh Zaritsky for useful discussions; François-Xavier Barre, Paula Bissichia, Nynke Dekker, Rodrigo Reyes-Lamothe, and David Sherratt for bacterial strains; and Da Yang and Scott Retterer for help in microfluidic chip making. The authors acknowledge the technical assistance of and material support from the Center for Environmental Biotechnology at the University of Tennessee. A part of this research was conducted at the Center for Nanophase Materials Sciences, which is sponsored at Oak Ridge National Laboratory by the Scientific User Facilities Division, Office of Basic Energy Sciences, US Department of Energy. This work has been supported by the US-Israel BSF research grant 2017004 (to Jaan Männik), the National Institutes of Health award under R01G M127413 (to Jaan Männik), NSF CAREER 1752024 (to A.A.), and NSF award 1806818 (to P.K.).

REFERENCES

- Aarsman MEG, Piette A, Fraipont C, Vinkenvleugel TMF, Nguyen-Disteche M, and den Blaauwen T (2005). Maturation of the *Escherichia coli* divisome occurs in two steps. *Mol. Microbiol* 55, 1631–1645. [PubMed: 15752189]
- Amir A (2014). Cell size regulation in bacteria. *Phys. Rev. Lett* 112, 208102.
- Baba T, Ara T, Hasegawa M, Takai Y, Okumura Y, Baba M, Datsenko KA, Tomita M, Wanner BL, and Mori H (2006). Construction of *Escherichia coli* K-12 in-frame, single-gene knockout mutants: the Keio collection. *Mol. Syst. Biol* 2, 1–11.
- Bailey MW, Bissichia P, Warren BT, Sherratt DJ, and Männik J (2014). Evidence for divisome localization mechanisms independent of the Min system and SlmA in *Escherichia coli*. *PLoS Genet.* 10, 1004504.
- Barber F, Amir A, and Murray AW (2020). Cell-size regulation in budding yeast does not depend on linear accumulation of Whi5. *Proc. Natl. Acad. Sci. U S A* 117, 14243–14250. [PubMed: 32518113]
- Barre FX, Aroyo M, Colloms SD, Helfrich A, Cornet F, and Sherratt DJ (2000). FtsK functions in the processing of a Holliday junction intermediate during bacterial chromosome segregation. *Genes Dev.* 14, 2976–2988. [PubMed: 11114887]

- Bates D, and Kleckner N (2005). Chromosome and replisome dynamics in *E. coli*: loss of sister cohesion triggers global chromosome movement and mediates chromosome segregation. *Cell* 121, 899–911. [PubMed: 15960977]
- Bernander R, and Nordstrom K (1990). Chromosome replication does not trigger cell division in *Escherichia coli*. *Cell* 60, 365–374. [PubMed: 2406019]
- Bernard R, Marquis KA, and Rudner DZ (2010). Nucleoid occlusion prevents cell division during replication fork arrest in *Bacillus subtilis*. *Mol. Microbiol* 78, 866–882. [PubMed: 20807205]
- Bernhardt TG, and de Boer PAJ (2005). SlmA, a nucleoid-associated, FtsZ binding protein required for blocking septal ring assembly over chromosomes in *E. coli*. *Mol. Cell* 18, 555–564. [PubMed: 15916962]
- Boes A, Olatunji S, Breukink E, and Terrak M (2019). Regulation of the peptidoglycan polymerase activity of PBP1b by antagonist actions of the core divisome proteins FtsBLQ and FtsN. *mBio*. 10, 01912–01918.
- Busiek KK, and Margolin W (2014). A role for FtsA in SPOR-independent localization of the essential *Escherichia coli* cell division protein FtsN. *Mol. Microbiol* 92, 1212–1226. [PubMed: 24750258]
- Cambridge J, Blinkova A, Magnan D, Bates D, and Walker JR (2014). A replication-inhibited unsegregated nucleoid at mid-cell blocks Z-ring formation and cell division independently of SOS and the SlmA nucleoid occlusion protein in *Escherichia coli*. *J. Bacteriol* 196, 36–49. [PubMed: 24142249]
- Campos M, Surovtsev IV, Kato S, Paintdakhi A, Beltran B, Ebmeier SE, and Jacobs-Wagner C (2014). A constant size extension drives bacterial cell size homeostasis. *Cell* 159, 1433–1446. [PubMed: 25480302]
- Cherepanov PP, and Wackernagel W (1995). Gene disruption in *Escherichia coli* - TcR and Km(R) cassettes with the option of flp-catalyzed excision of the antibiotic-resistance determinant. *Gene*. 158, 9–14. [PubMed: 7789817]
- Cho HB, McManus HR, Dove SL, and Bernhardt TG (2011). Nucleoid occlusion factor SlmA is a DNA-activated FtsZ polymerization antagonist. *Proc. Natl. Acad. Sci. U S A* 108, 3773–3778. [PubMed: 21321206]
- Colin A, Micali G, Faure L, Lagomarsino MC, and van Teeffelen S (2021). Two different cell-cycle processes determine the timing of cell division in *Escherichia coli*. *eLife* 10, e67495. [PubMed: 34612203]
- Cooper S, and Helmstetter CE (1968). Chromosome replication and division cycle of *Escherichia coli* B/r. *J. Mol. Biol* 31, 519–540. [PubMed: 4866337]
- Daley DO, Skoglund U, and Soderstrom B (2016). FtsZ does not initiate membrane constriction at the onset of division. *Sci. Rep* 6, 33138. [PubMed: 27609565]
- Datsenko KA, and Wanner BL (2000). One-step inactivation of chromosomal genes in *Escherichia coli* K-12 using PCR products. *Proc. Natl. Acad. Sci. U S A* 97, 6640–6645. [PubMed: 10829079]
- de Boer PAJ (2010). Advances in understanding *E. coli* cell fission. *Curr. Opin. Microbiol* 13, 730–737. [PubMed: 20943430]
- Du SS, and Lutkenhaus J (2019). At the heart of bacterial cytokinesis: the Z ring. *Trends Microbiol*. 27, 781–791. [PubMed: 31171437]
- Egan AJF, Errington J, and Vollmer W (2020). Regulation of peptidoglycan synthesis and remodelling. *Nat. Rev. Microbiol* 18, 446–460. [PubMed: 32424210]
- Espeli O, Borne R, Dupaigne P, Thiel A, Gigant E, Mercier R, and Boccard F (2012). A MatP-divisome interaction coordinates chromosome segregation with cell division in *E. coli*. *EMBO J*. 31, 3198–3211. [PubMed: 22580828]
- Eun YJ, Ho PY, Kim M, LaRussa S, Robert L, Renner LD, Schmid A, Garner E, and Amir A (2018). Archaeal cells share common size control with bacteria despite noisier growth and division. *Nat. Microbiol* 3, 148–154. [PubMed: 29255255]
- Galli E, Midonet C, Paly E, and Barre FX (2017). Fast growth conditions uncouple the final stages of chromosome segregation and cell division in *Escherichia coli*. *PLoS Genet*. 13, 1006702.
- Haeusser DP, and Margolin W (2016). Splitsville: structural and functional insights into the dynamic bacterial Z ring. *Nat. Rev. Microbiol* 14, 305–319. [PubMed: 27040757]

- Harris LK, and Theriot JA (2016). Relative rates of surface and volume synthesis set bacterial cell size. *Cell* 165, 1479–1492. [PubMed: 27259152]
- Herendeen SL, Vanbogelen RA, and Neidhardt FC (1979). Levels of major proteins of *Escherichia coli* during growth at different temperatures. *J. Bacteriol* 139, 185–194. [PubMed: 156716]
- Ho P-Y, and Amir A (2015). Simultaneous regulation of cell size and chromosome replication in bacteria. *Front. Microbiol* 6, 662. [PubMed: 26217311]
- Ho P-Y, Lin J, and Amir A (2018). Modeling cell size regulation: from single-cell-level statistics to molecular mechanisms and population-level effects. *Annual Review of Biophysics* 46, 251–271.
- Joshi MC, Bourniquel A, Fisher J, Ho BT, Magnan D, Kleckner N, and Bates D (2011). *Escherichia coli* sister chromosome separation includes an abrupt global transition with concomitant release of late-splitting intersister snaps. *Proc. Natl. Acad. Sci. U. S. A* 108, 2765–2770. [PubMed: 21282646]
- Katayama T, Kasho K, and Kawakami H (2017). The DnaA cycle in *Escherichia coli*: activation, function and inactivation of the initiator protein. *Front. Microbiol* 8, 2496. [PubMed: 29312202]
- Kennedy SP, Chevalier F, and Barre F-X (2008). Delayed activation of Xer recombination at *dif* by FtsK during septum assembly in *Escherichia coli*. *Mol. Microbiol* 68, 1018–1028. [PubMed: 18363794]
- Liu B, Persons L, Lee L, and de Boer PAJ (2015). Roles for both FtsA and the FtsBLQ subcomplex in FtsN-stimulated cell constriction in *Escherichia coli*. *Mol. Microbiol* 95, 945–970. [PubMed: 25496160]
- Logsdon MM, Ho PY, Papavinasasundaram K, Richardson K, Cokol M, Sassetti CM, Amir A, and Aldridge BB (2017). A parallel adder coordinates mycobacterial cell-cycle progression and cell-size homeostasis in the context of asymmetric growth and organization. *Curr. Biol* 27, 3367. [PubMed: 29107550]
- Männik J, and Bailey MW (2015). Spatial coordination between chromosomes and cell division proteins in *Escherichia coli*. *Front. Microbiol* 6, 306. [PubMed: 25926826]
- Männik J, Bailey MW, O’Neill JC, and Männik J (2017). Kinetics of large-scale chromosomal movement during asymmetric cell division in *Escherichia coli*. *PLoS Genet.* 13, e1006638. [PubMed: 28234902]
- Männik J, Castillo D, Yang D, Siopsis G, and Männik J (2016). The role of MatP, ZapA, and ZapB in chromosomal organization and dynamics in *Escherichia coli*. *Nucleic Acids Res.* 44, 1216–1226. [PubMed: 26762981]
- Männik J, Walker BE, and Männik J (2018). Cell cycle-dependent regulation of FtsZ in *Escherichia coli* in slow growth conditions. *Mol. Microbiol* 110, 1030–1044. [PubMed: 30230648]
- Micali G, Grilli J, Marchi J, Osella M, and Lagomarsino MC (2018a). Dissecting the control mechanisms for DNA replication and cell division in *E. coli*. *Cell Rep.* 25, 761–771. [PubMed: 30332654]
- Micali G, Grilli J, Osella M, and Lagomarsino MC (2018b). Concurrent processes set *E. coli* cell division. *Sci. Adv* 4, 3324.
- Moolman MC, Krishnan ST, Kerssemakers JWJ, van den Berg A, Tulinski P, Depken M, Reyes-Lamothe R, Sherratt DJ, and Dekker NH (2014). Slow unloading leads to DNA-bound beta(2)-sliding clamp accumulation in live *Escherichia coli* cells. *Nat. Commun* 5, 11.
- Mulder E, and Woldringh CL (1989). Actively replicating nucleoids influence positioning of division sites in *Escherichia coli* filaments forming cells lacking DNA. *J. Bacteriol* 171, 4303–4314. [PubMed: 2666394]
- Nicholls A (2014). Confidence limits, error bars and method comparison in molecular modeling. Part 1: the calculation of confidence intervals. *J. Computer-Aided Mol. Des* 28, 887–918.
- Nielsen HJ, Li YF, Youngren B, Hansen FG, and Austin S (2006). Progressive segregation of the *Escherichia coli* chromosome. *Mol. Microbiol* 61, 383–393. [PubMed: 16771843]
- Rao TVP, and Kuzminov A (2020). Exopolysaccharide defects cause hyper-thymineless death in *Escherichia coli* via massive loss of chromosomal DNA and cell lysis. *Proc. Natl. Acad. Sci. U S A* 117, 33549–33560. [PubMed: 33318216]
- Reshes G, Vanounou S, Fishov I, and Feingold M (2008). Cell shape dynamics in *Escherichia coli*. *Biophys. J* 94, 251–264. [PubMed: 17766333]

- Reyes-Lamothe R, Possoz C, Danilova O, and Sherratt DJ (2008). Independent positioning and action of *Escherichia coli* replisomes in live cells. *Cell* 133, 90–102. [PubMed: 18394992]
- Reyes-Lamothe R, and Sherratt DJ (2019). The bacterial cell cycle, chromosome inheritance and cell growth. *Nat. Rev. Microbiol* 17, 467–478. [PubMed: 31164753]
- Reyes-Lamothe R, Sherratt DJ, and Leake MC (2010). Stoichiometry and architecture of active DNA replication machinery in *Escherichia coli*. *Science* 328, 498–501. [PubMed: 20413500]
- Rodrigues CDA, and Harry EJ (2012). The Min system and nucleoid occlusion are not required for identifying the division site in *Bacillus subtilis* but ensure its efficient utilization. *PLoS Genet.* 8, 1002561.
- Sherratt DJ, Arciszewska LK, Crozat E, Graham JE, and Grainge I (2010). The *Escherichia coli* DNA translocase FtsK. *Biochem. Soc. Trans* 38, 395–398. [PubMed: 20298190]
- Si FW, Le Treut G, Sauls JT, Vadia S, Levin PA, and Jun S (2019). Mechanistic origin of cell-size control and homeostasis in bacteria. *Curr. Biol* 29, 1–11. [PubMed: 30581019]
- Soderstrom B, Chan H, Shilling PJ, Skoglund U, and Daley DO (2018). Spatial separation of FtsZ and FtsN during cell division. *Mol. Microbiol* 107, 387–401. [PubMed: 29193432]
- Soifer I, Robert L, and Amir A (2016). Single-cell analysis of growth in budding yeast and bacteria reveals a common size regulation strategy. *Curr. Biol* 26, 356–361. [PubMed: 26776734]
- Stouf M, Meile J-C, and Cornet F (2013). FtsK actively segregates sister chromosomes in *Escherichia coli*. *Proc. Natl. Acad. Sci. U S A* 110, 11157–11162. [PubMed: 23781109]
- Taheri-Araghi S, Bradde S, Sauls JT, Hill NS, Levin PA, Paulsson J, Vergassola M, and Jun S (2015). Cell-size control and homeostasis in bacteria. *Curr. Biol* 25, 385–391. [PubMed: 25544609]
- Trueba FJ, Neijssel OM, and Woldringh CL (1982). Generality of the growth-kinetics of the average individual cell in different bacterial-populations. *J. Bacteriol* 150, 1048–1055. [PubMed: 6804435]
- Walker BE, Mannik J, and Mannik J (2020). Transient membrane-linked FtsZ assemblies precede Z-ring formation in *Escherichia coli*. *Curr. Biol* 30, 499–508. [PubMed: 31978334]
- Wallden M, Fange D, Lundius EG, Baltekin O, and Elf J (2016). The synchronization of replication and division cycles in individual *E. coli* cells. *Cell* 166, 729–739. [PubMed: 27471967]
- Wang P, Robert L, Pelletier J, Dang WL, Taddei F, Wright A, and Jun S (2010). Robust growth of *Escherichia coli*. *Curr. Biol* 20, 1099–1103. [PubMed: 20537537]
- Weiss DS (2015). Last but not least: new insights into how FtsN triggers constriction during *Escherichia coli* cell division. *Mol. Microbiol* 95, 903–909. [PubMed: 25571948]
- Wery M, Woldringh CL, and Rouviere-Yaniv J (2001). HU-GFP and DAPI co-localize on the *Escherichia coli* nucleoid. *Biochimie* 83, 193–200. [PubMed: 11278069]
- Willis L, and Huang KC (2017). Sizing up the bacterial cell cycle. *Nat. Rev. Microbiol* 15, 606–620. [PubMed: 28804128]
- Witz G, van Nimwegen E, and Julou T (2019). Initiation of chromosome replication controls both division and replication cycles in *E. coli* through a double-adder mechanism. *eLife* 8, 48063.
- Woldringh CL, Hansen FG, Vischer NOE, and Atlung T (2015). Segregation of chromosome arms in growing and non-growing *Escherichia coli* cells. *Front. Microbiol* 6, 448. [PubMed: 26029188]
- Yang D, Jennings AD, Borrego E, Retterer ST, and Männik J (2018). Analysis of factors limiting bacterial growth in PDMS mother machine devices. *Front. Microbiol* 9, 871. [PubMed: 29765371]
- Youngren B, Nielsen HJ, Jun S, and Austin S (2014). The multifork *Escherichia coli* chromosome is a self-duplicating and self-segregating thermodynamic ring polymer. *Genes Dev.* 28, 71–84. [PubMed: 24395248]
- Zaritsky A, Woldringh CL, Einav M, and Alexeeva S (2006). Use of thymine limitation and thymine starvation to study bacterial physiology and cytology. *J. Bacteriol* 188, 1667–1679. [PubMed: 16484178]

Highlights

- The unreplicated chromosome blocks the onset of constriction at mid-cell in *E. coli*
- The blockage is lifted at about the time of replication termination
- The nucleoid occlusion protein SlmA is not directly involved in this process
- The effect is limiting cell division at slow growth rates

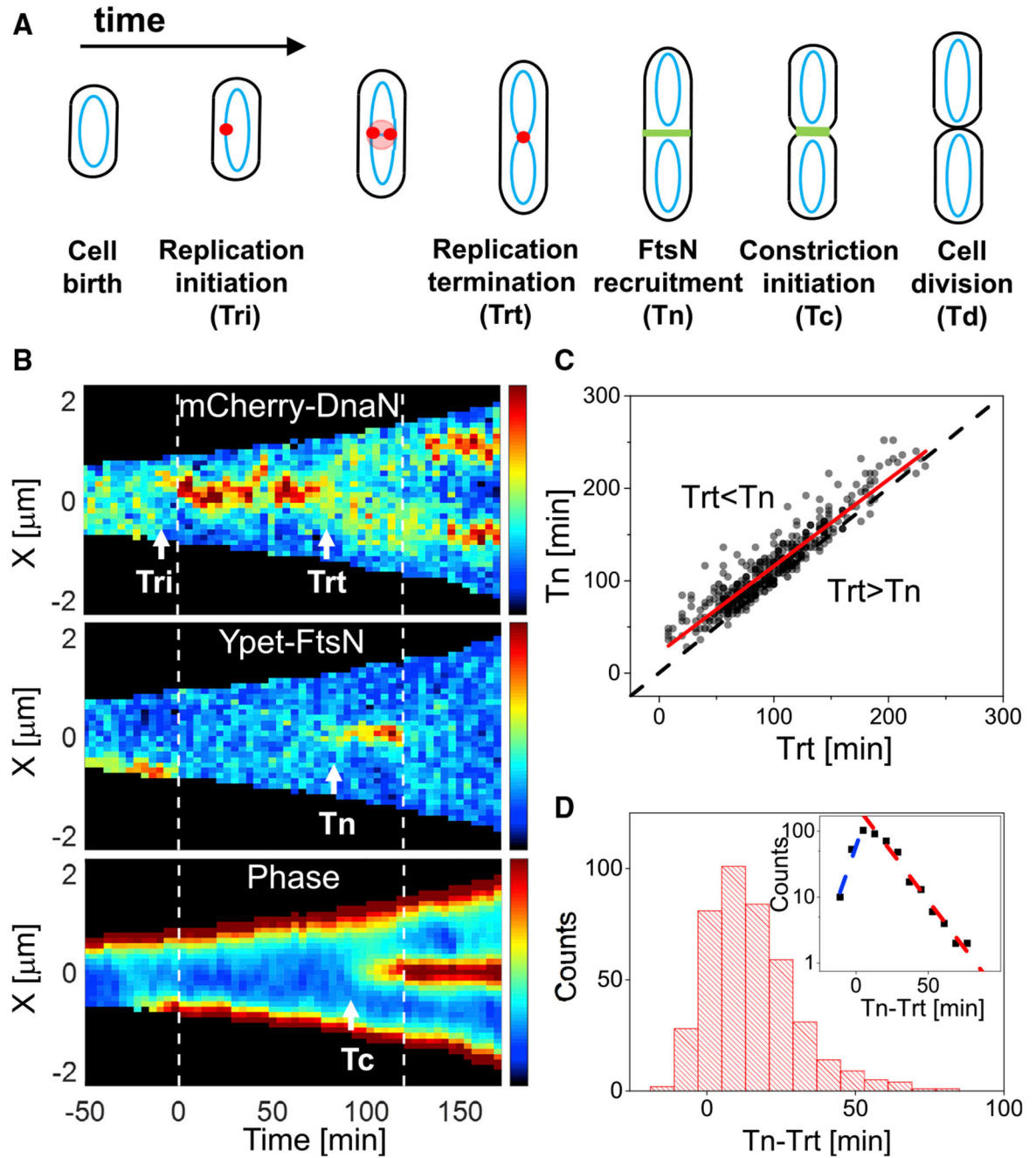


Figure 1. Timing of constriction formation and recruitment of FtsN relative to the termination of replication in slow growth conditions

(A) Schematics for the main cell-cycle events and timings that are determined from time-lapse measurements.

(B) Kymographs of fluorescent and phase signals for a representative cell grown in M9 glycerol medium. Dashed vertical lines indicate cell division events. Red corresponds to high- and blue to low-intensity values. Event timings are indicated by arrows.

(C) Termination of replication (Trt) versus initiation of constriction (Tn) for a population of cells ($n = 420$). Tn is determined based on the accumulation of Ypet-FtsN signal at

mid-cell. The solid red line is a linear fit with ($Tn = 0.94 Trt + 22$ min). The dashed black line corresponds to $Trt = Tn$.

(D) Distribution of delay times between constriction formation and termination of replication for these cells. The inset shows the same data in a semi-logarithmic plot. The dashed lines are fits to exponential decay. The time constant for the fit at negative times is 7 min and for positive times 15 min.

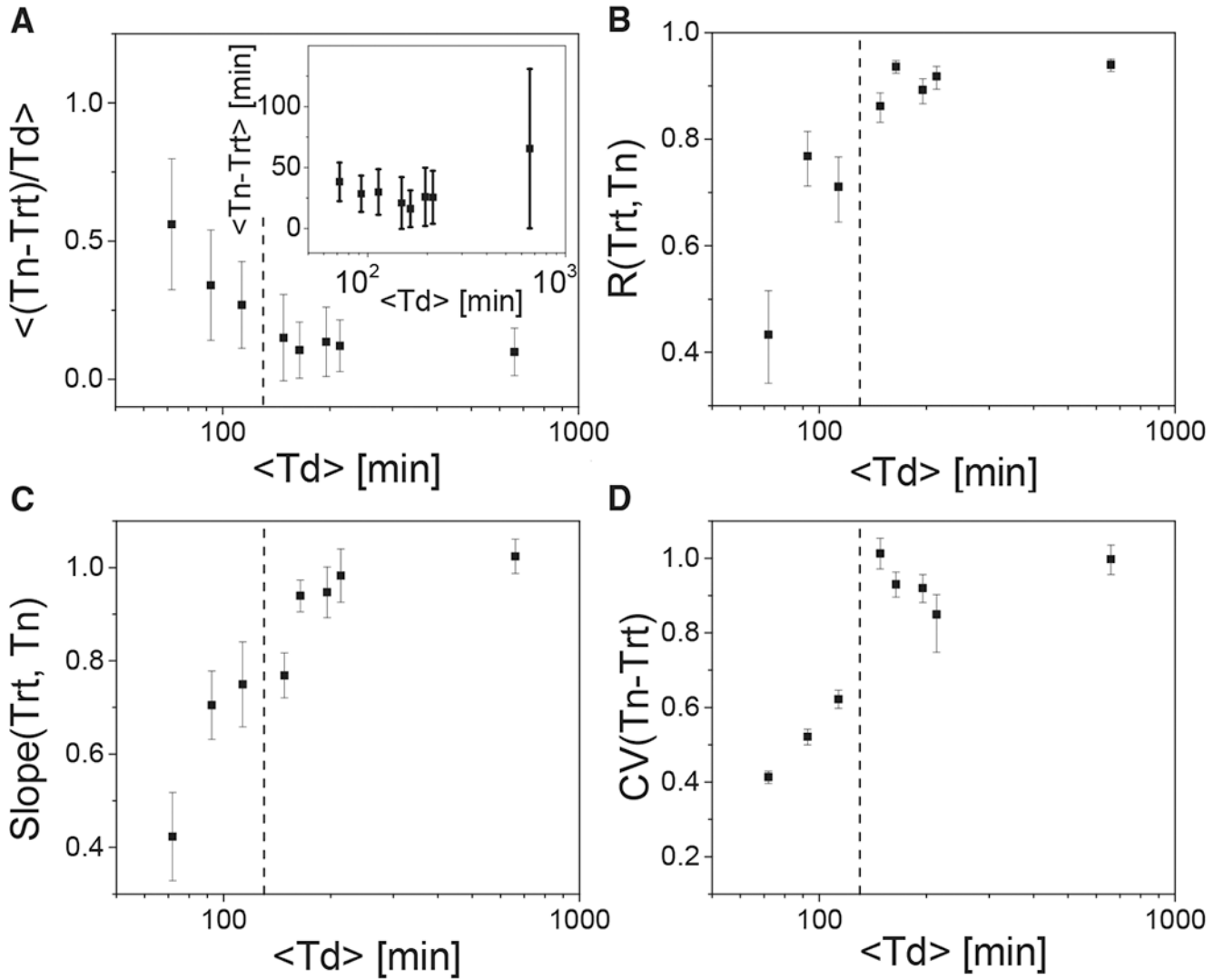


Figure 2. Comparison of timings of constriction initiation and termination of replication in eight different growth media

From the longest to shortest doubling times, the carbon sources used in the media are acetate, alanine, mannose, glycerol, glycerol + trace elements (TrEl), glucose, glycerol-Cas, and glucose-Cas (for details, see Table S4).

(A) The average normalized delay time between initiation of constriction and termination of replication as a function of the average doubling time, T_d . The inset shows the unnormalized delay time. The error bars in both plots show the SDs of these quantities within the cell population.

(B) Pearson correlation coefficient between Trt and T_n .

(C) The slope of Trt versus T_n plot.

(D) Coefficient of variation for $Trt - T_n$ distribution. The dashed vertical lines in all of the plots correspond to $T_d = 130$ min. The error bars in (B)–(D) show 95% confidence intervals. For the calculation of these intervals, see Method details.

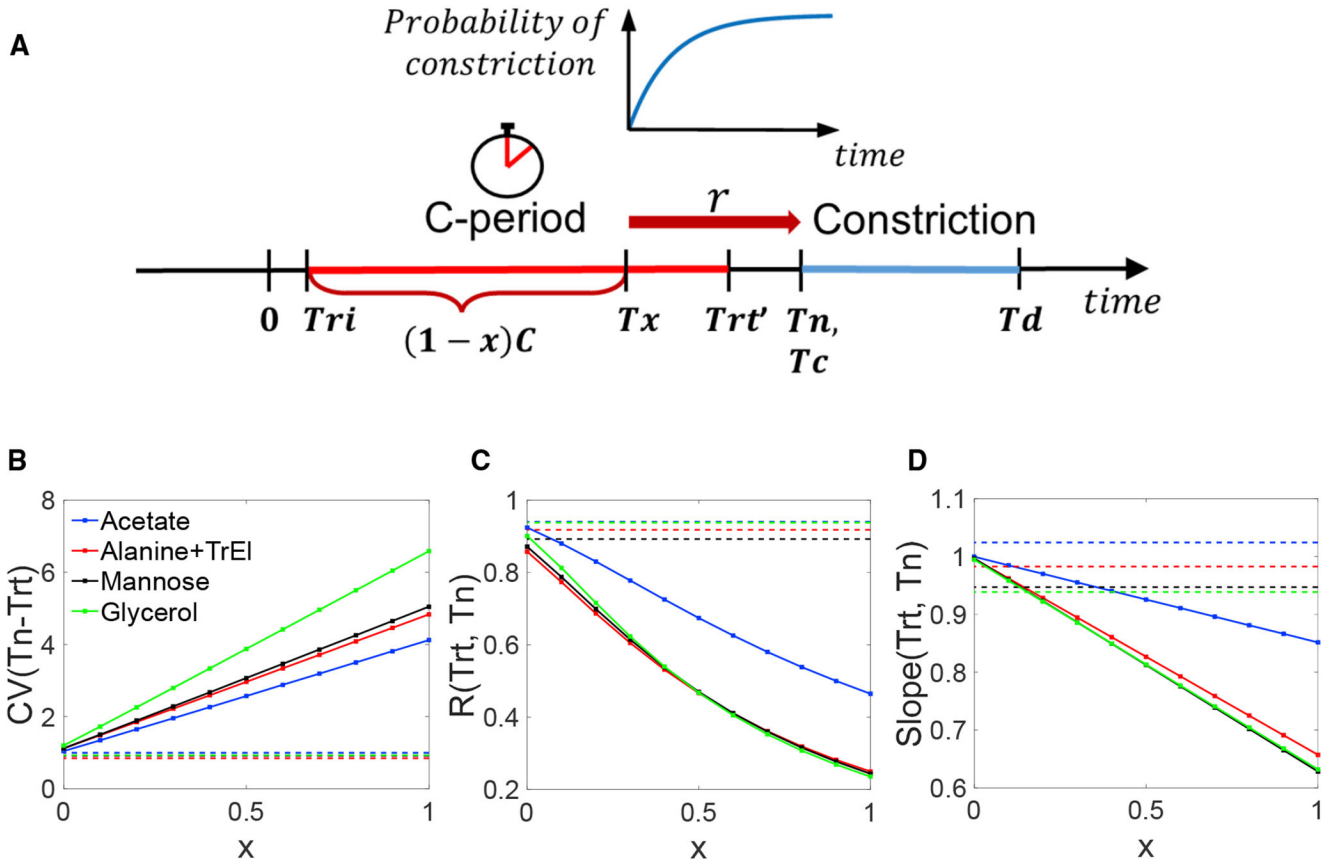


Figure 3. Predictions of the model coupling the replication cycle to the onset of constriction

(A) Schematics representing the model. T_x is the timing for the checkpoint that triggers constriction formation. x is the normalized time of this checkpoint from termination. T_{rt}' is the actual time of termination, which differs from the measured time T_{rt} by the detachment time of mCherry-DnaN from the chromosome (see Method details).

(B) Coefficient of variation of the $T_n - T_{rt}$ distribution.

(C and D) Pearson correlation coefficient between T_{rt} and T_n (C) and (D) the slope of the linear regression line for T_n versus T_{rt} plotted as a function of x .

In (B)–(D), the solid lines show predictions of the model and the dashed horizontal lines show the experimental values. Note that only the four slowest growth conditions are considered in these comparisons and attachment time of DnaN to DNA, $T_a=3$ min. The calculated curves for $T_a=6$ min are almost indistinguishable from those for $T_a=3$ min.

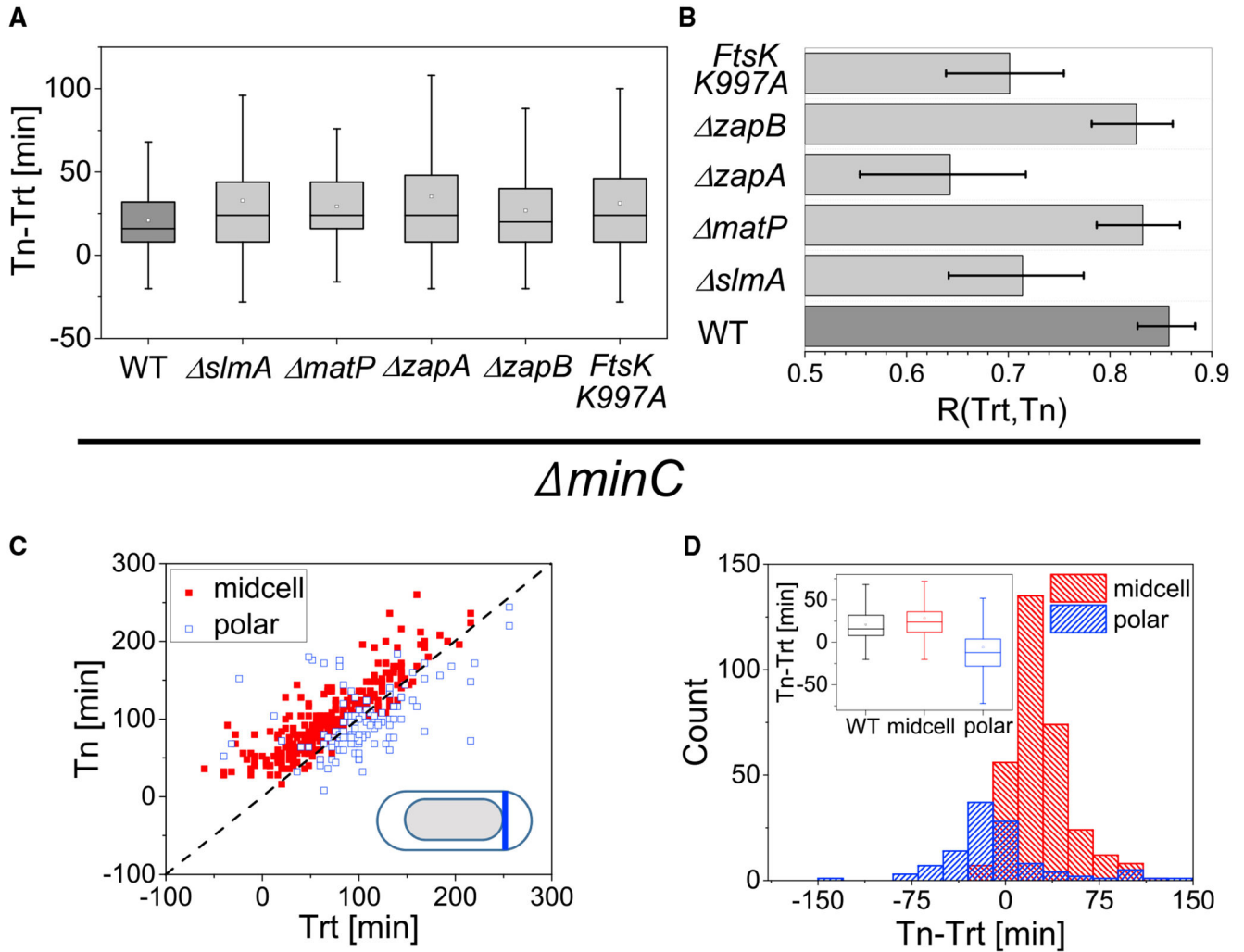


Figure 4. Timings for the termination of replication and constriction initiation for different deletion mutants

The deleted gene products have been implicated in coordinating the Z ring formation and replication processes.

(A) Delay times between the termination and initiation of constriction for wild-type (WT), *slmA*, *matP*, *zapA*, *zapB*, and *ftsK K997A* strains. All of the mutant strains show longer delay times than the WT strain at the $p = 0.05$ level (t test; Table S6).

(B) Pearson correlation coefficients between these times for the same strains. Error bars reflect 95% confidence intervals.

(C) Termination of replication (*Trt*) versus initiation of constriction (*Tn*) for *minC* cells. Polar divisions and mid-cell divisions are separately labeled.

(D) Distribution of corresponding delay times in this strain. The inset compares the distributions to the corresponding one in WT cells. All the measurements were performed in M9 glycerol-TrEI medium.

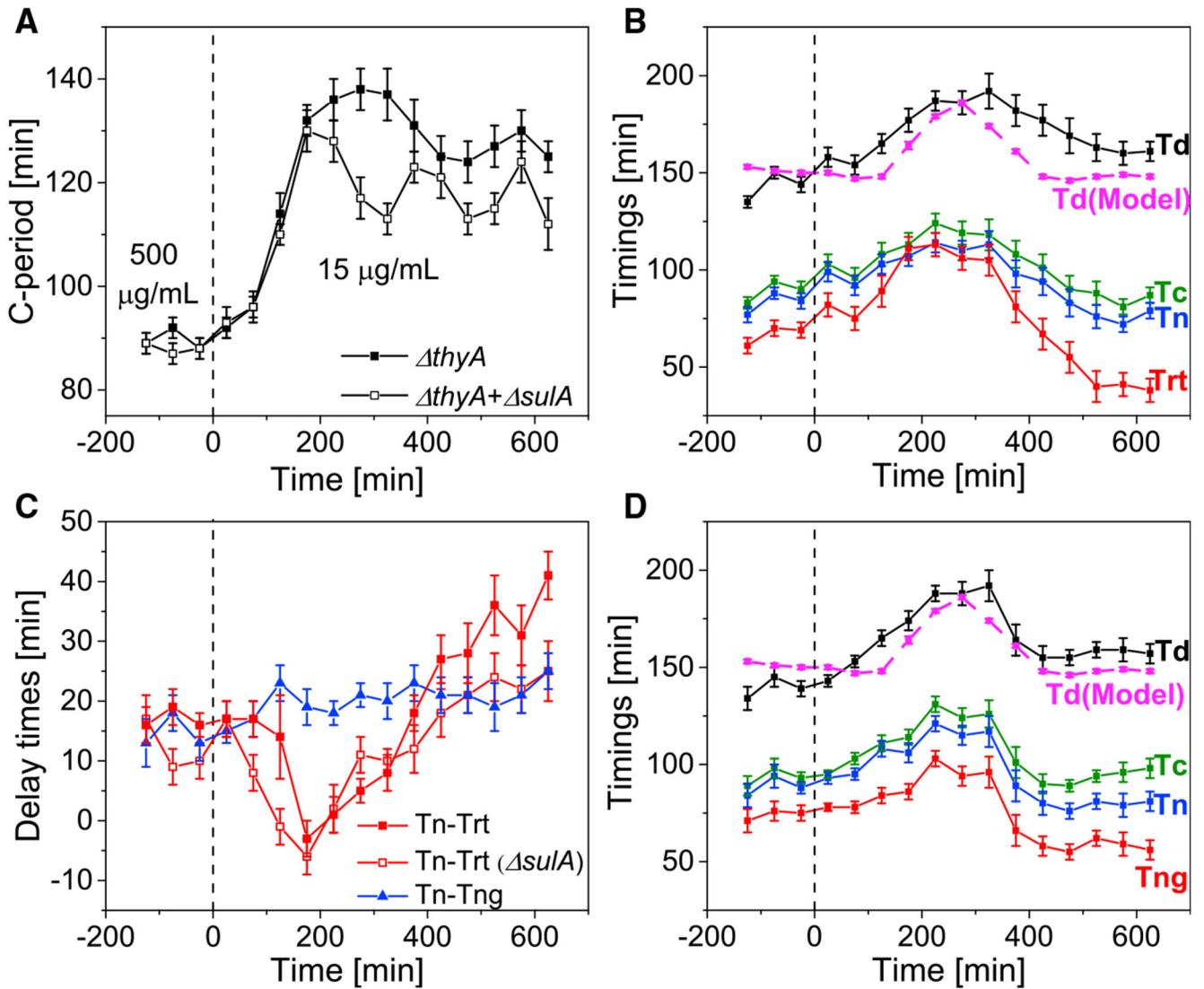


Figure 5. Transient changes in DNA replication and division timings upon thymine step-down from 500 to 15 µg/ml

(A) Increase in replication period (C-period) upon the change in thymine concentration in *thyA* (strain STK37) and *thyA + sulA* (STK39) strains as a function of time relative to cell division. Time zero corresponds to thymine step-down (indicated by a dashed vertical line).

(B) Doubling time (*Td*), termination of replication (*Trt*), and initiation of constriction (*Tn*, *Tc*) as a function of time in the *thyA* strain. For a better comparison, all of the timings are plotted relative to the time when the cell divides and then the data are binned along the time axes. The pink dashed line shows *Td* calculated based on the adder per origin model (see Method details).

(C) Delay times *Tn – Trt* and *Tn – Tng* before and after thymine step-down. *Tng* corresponds to the first detectable decrease in nucleoid density at the cell middle and is determined using the fluorescence signal from the HupA-mCherry label (strain STK46). For the determination of *Tng*, see Method details and Figure S6E.

(D) T_d , T_{ng} , T_{rt} , T_c , and T_n as a function of time (strain STK46). All of the measurements were done in glycerol + TrEI medium (Table S4). The error bars correspond to standard error.

Author Manuscript

Author Manuscript

Author Manuscript

Author Manuscript

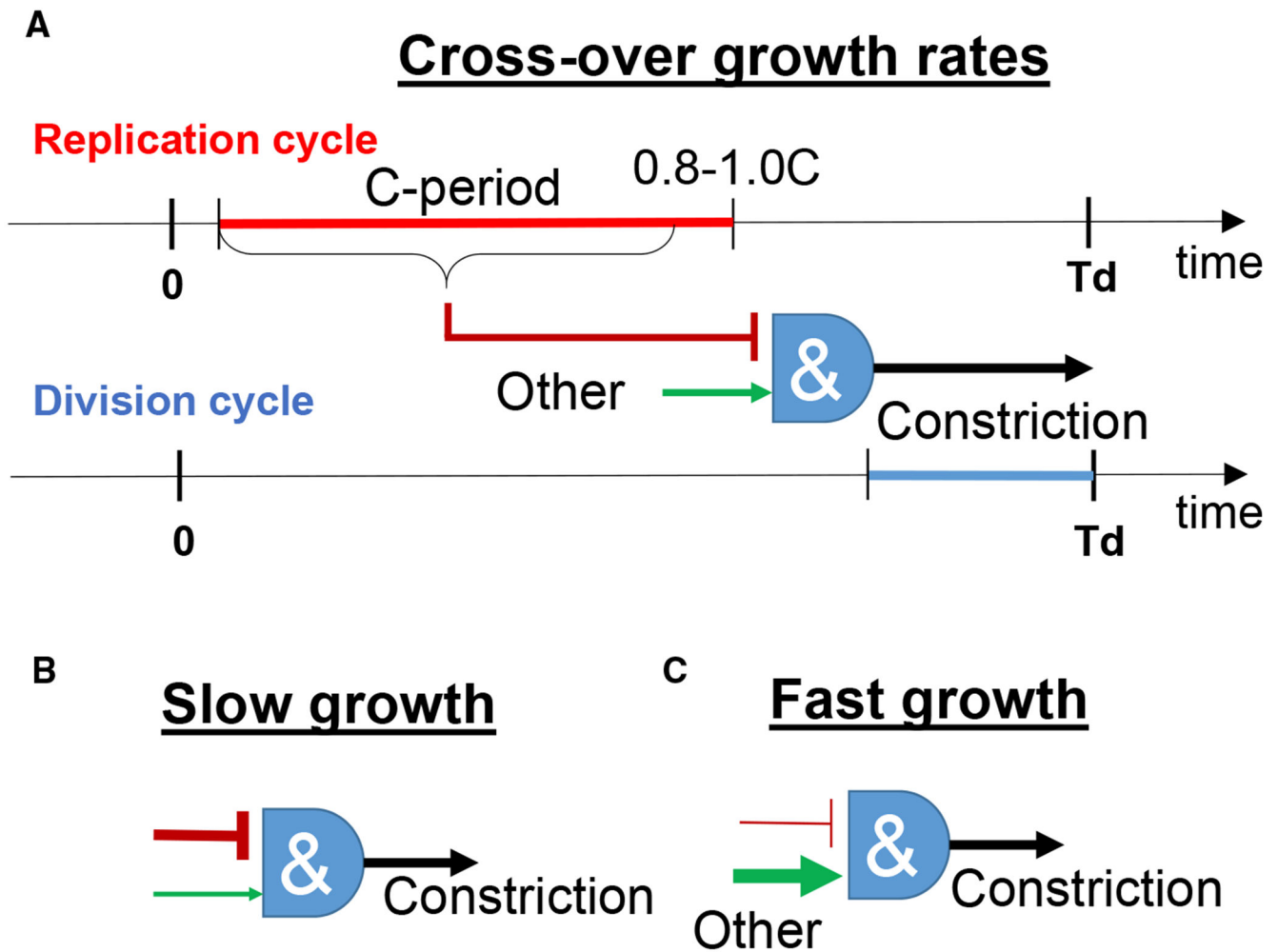


Figure 6. Regulation of constriction formation in different growth rates

(A) Regulation at the crossover regime at which $Td \approx 130$ min. The corresponding doubling times at 37°C are expected to be approximately 2 times shorter. The replication period is shown by red and the constriction period by blue lines. The & sign indicates an integration of different signals. Constriction starts when conditions imposed by some form of nucleoid occlusion in a replication-dependent manner and by some other, yet to be identified process(es) have both been met. Replication-related processes relieve inhibition for the initiation of constriction at or shortly before the termination (–). The exact origin of the "other" processes is unknown, but for definiteness, they are shown to positively regulate the onset of constriction (→).

(B) In slow-growth conditions, the onset of constriction is rate limited by replication-related processes. The condition imposed by the "other" processes was met earlier. The sign in bold indicates the limiting process.

(C) In fast-growth conditions, the condition for replication-related processes is already met in the early cell cycle, while the "other" processes are limiting.

KEY RESOURCES TABLE

REAGENT or RESOURCE	SOURCE	IDENTIFIER
Bacterial and virus strains		
See Table S1		N/A
Chemicals, peptides, and recombinant proteins		
Chloramphenicol (CM)	MilliporeSigma	Cat#C0378-5G
Kanamycin (Kan)	MilliporeSigma	Cat#K4000-5G
Ampicillin	MilliporeSigma	Cat#A0166-5G
Glucose	MilliporeSigma	Cat#G8270-100G
Glycerol	Fisher BioReagents	Cat#BP229-1
Alanine	Fisher BioReagents	Cat#BP369-100
Mannose	MilliporeSigma	Cat#M6020-25G
Sodium acetate (acetate)	MilliporeSigma	Cat#S5636-250G
Casamino acids (Cas)	ACROS Organics	Cat#AC612041000
Thymine	MP Biomedicals	Cat#0210306025
Isopropanol	Fisher Chemical	Cat#A464-4
Bovine Serum Albumin (BSA)	MilliporeSigma	Cat#A7906-10G
M9 minimal media	Teknova.com	Cat#M1902
Trace metal elements mixture	Teknova.com	Cat#T1001
Sylgard 184 Silicone Elastomer Kit	Dow Inc.	N/A
Deposited data		
Experimental data	This paper	Mendeley Data: https://doi.org/10.17632/hwzcywsc4.1
Code used in modeling of coupling between DNA replication and the initiation of constriction in <i>E. coli</i>	This paper	GitHub: https://doi.org/10.5281/zenodo.6113652
Oligonucleotides		
See Table S2		N/A
Software and algorithms		
MATLAB R2017a	Mathworks, Inc	RRID:SCR_001622
NIS-Elements	Nikon Instruments Inc.	RRID:SCR_014329
DipImage toolboxes	http://www.diplib.org/	N/A
Python 3.7	https://www.python.org	RRID:SCR_008394
Other		
Nikon Ti-E inverted microscope	Nikon Instruments Inc.	Cat# MEA53100
Nikon Perfect Focus system	Nikon Instruments Inc.	Cat# MEP59390
Andor EMCCD camera	Oxford Instruments	iXon897
O ₂ plasma asher	March Instruments	Plasmod
Syringe pump	New Era Pump Systems	Model: NE-1000
Syringe pump	New Era Pump Systems	Model: NE-2000